



Fluid-Driven Instabilities in Granular Media: From Viscous Fingering and Dissolution Wormholes to Desiccation Cracks and Ice Lenses

Qi Liu and J. Carlos Santamarina*

KAUST King Abdullah University of Science and Technology, Thuwal, Saudi Arabia

Single and multi-phase fluids fill the pore space in sediments; phases may include gases (air, CH₄, CO₂, H₂, and NH₃), liquids (aqueous solutions or organic compounds), and even ice and hydrates. Fluids can experience instabilities within the pore space or trigger instabilities in the granular skeleton. Then, we divided fluid-driven instabilities in granular media into two categories. Fluid instabilities at constant fabric take place within the pore space without affecting the granular skeleton; these can result from hysteresis in contact angle and interfacial tension (aggravated in particle-laden flow), fluid compressibility, changes in pore geometry along the flow direction, and contrasting viscosity among immiscible fluids. More intricate fluid instabilities with fabric changes take place when fluids affect the granular skeleton, thus the evolving local effective stress field. We considered several cases: 1) open-mode discontinuities driven by drag forces, i.e., hydraulic fracture; 2) grain-displacive invasion of immiscible fluids, such as desiccation cracks, ice and hydrate lenses, gas and oil-driven openings, and capillary collapse; 3) hydro-chemo-mechanically coupled instabilities triggered by mineral dissolution during the injection of reactive fluids, from wormholes to shear band formation; and 4) instabilities associated with particle transport (backward piping erosion), thermal changes (thermo-hydraulic fractures), and changes in electrical interparticle interaction (osmotic-hydraulic fractures and contractive openings). In all cases, we seek to identify the pore and particle-scale positive feedback mechanisms that amplify initial perturbations and to identify the governing dimensionless ratios that define the stable and unstable domains. A [N/m] Contact line adhesion

Keywords: multi-phase fluid, capillary phenomena, reactive flow, particle-laden flow, instability, THCM coupling

1 INTRODUCTION

Contrary to the generalized use of equivalent continuum models, instabilities often emerge and determine the macroscale response of granular materials. They can result from mechanical actions (e.g., shear and compaction bands) or from coupled processes such as hydro-mechanically coupled hydraulic fractures or chemo-mechanically coupled contraction cracks. Multi-phase fluids add additional mechanisms that can result in pore-scale and macro-scale instabilities, from Haines jumps to segregated ice lenses and giant desiccation cracks.

OPEN ACCESS

Edited by:

Giulio Sciarra,
Ecole Centrale de Nantes, France

Reviewed by:

Alexandre Guevel,
Duke University, United States
Alessandro Tarantino,
University of Strathclyde,
United Kingdom

*Correspondence:

J. Carlos Santamarina
carlos.santamarina@kaust.edu.sa

Specialty section:

This article was submitted to
Solid and Structural Mechanics,
a section of the journal
Frontiers in Mechanical Engineering

Received: 24 January 2022

Accepted: 26 May 2022

Published: 08 July 2022

Citation:

Liu Q and Santamarina J (2022) Fluid-Driven Instabilities in Granular Media: From Viscous Fingering and Dissolution Wormholes to Desiccation Cracks and Ice Lenses. *Front. Mech. Eng* 8:861554. doi: 10.3389/fmech.2022.861554

TABLE 1 | Fluid-driven instabilities in granular materials. Examples are organized into instabilities 1) at constant fabric and 2) with fabric changes.

Fluid instabilities at constant fabric	Single-phase fluids	Thermal-viscous fingering Thermal convection Double-diffusion convection
	Multi-phase fluids	Stick-slip interface displacement due to contact line pinning Buckling of the particle-coated fluid-fluid interface Haines jump and snap-off: elastocapillarity Capillary fingering Viscous fingering
	Particle-laden fluids	Clogging ring formation in convergent radial flow (Note: stable and self-homogenizing) Localized fine erosion, i.e., suffusion Frictional stick-slip patterns (dense suspension and fluids with yield stress)
	Reactive fluids	Rayleigh–Taylor instability at the suspension-solvent interface Precipitation (Note: stable and self-homogenizing) Dissolution, e.g., wormholes
Fluid instabilities with fabric changes	Single-phase fluids	Drag-driven open-mode discontinuities, i.e., “hydraulic fracture”
	Multi-phase fluids	Capillary-driven open-mode discontinuities, e.g., “desiccation cracks” Self-driven buoyant fluids, i.e., cavity expansion, fractures, pipes, pockmarks Grain-displacive ice and hydrate lenses Instabilities during imbibition: volumetric collapse and peripheral cracks
	Particle-laden fluids	Piping by backward erosion Sand dikes: migration from the lower liquefied layer through the discontinuous upper layer Mud volcano: mud flow to the surface often driven by pressurized hydrocarbons
	Reactive fluids	Settlement and void ratio increase toward e_{max} → brittle granular skeleton Horizontal stress drop can reach Rankine’s active K_a , i.e., failure Pressure solution may cause shear localization (resulting in polygonal faulting)
	Increased ionic activity	DLVO interaction and volume contraction: internal fracturing of clay sediments

Instabilities can determine deformation and pressure fields and control fluid transport and the “geo-plumbing” of the formation. Furthermore, instabilities affect the upscaling of laboratory results to the field and all engineering analyses and designs such as foundations, subsurface structures, resource recovery and geological storage.

At the macro-scale, instabilities imply a non-convex potential energy surface (Kochmann and Bertoldi, 2017). At the particle/pore-scale, instabilities involve positive feedback mechanisms that exacerbate the effects of initial perturbations.

Table 1 compiles observed/reported fluid-driven instabilities that take place at constant fabric or cause fabric changes. The following sections analyze the evolution of such fluid-driven instabilities in granular materials to identify underlying pore and particle scale processes. We conducted cast analyses within the framework of particle/pore scale dimensionless ratios to identify the governing parameters that define stable and unstable regimes.

2 FLUID INSTABILITIES AT CONSTANT FABRIC

We first consider the various forms of instabilities that emerge during fluid invasion/flow through a rigid porous medium, i.e., without mechanical coupling. We explore single and multi-phase fluids, particle-laden fluids, and reactive fluids.

2.1 Multi-Phase Fluids

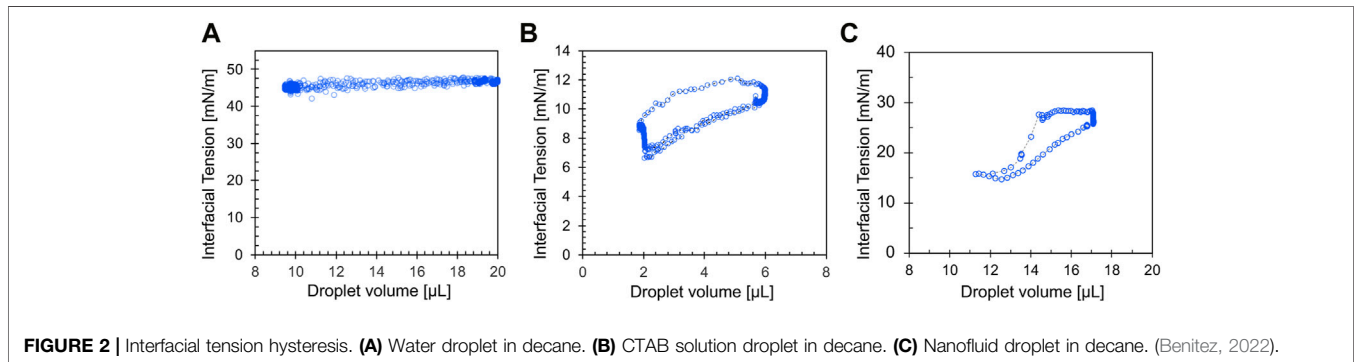
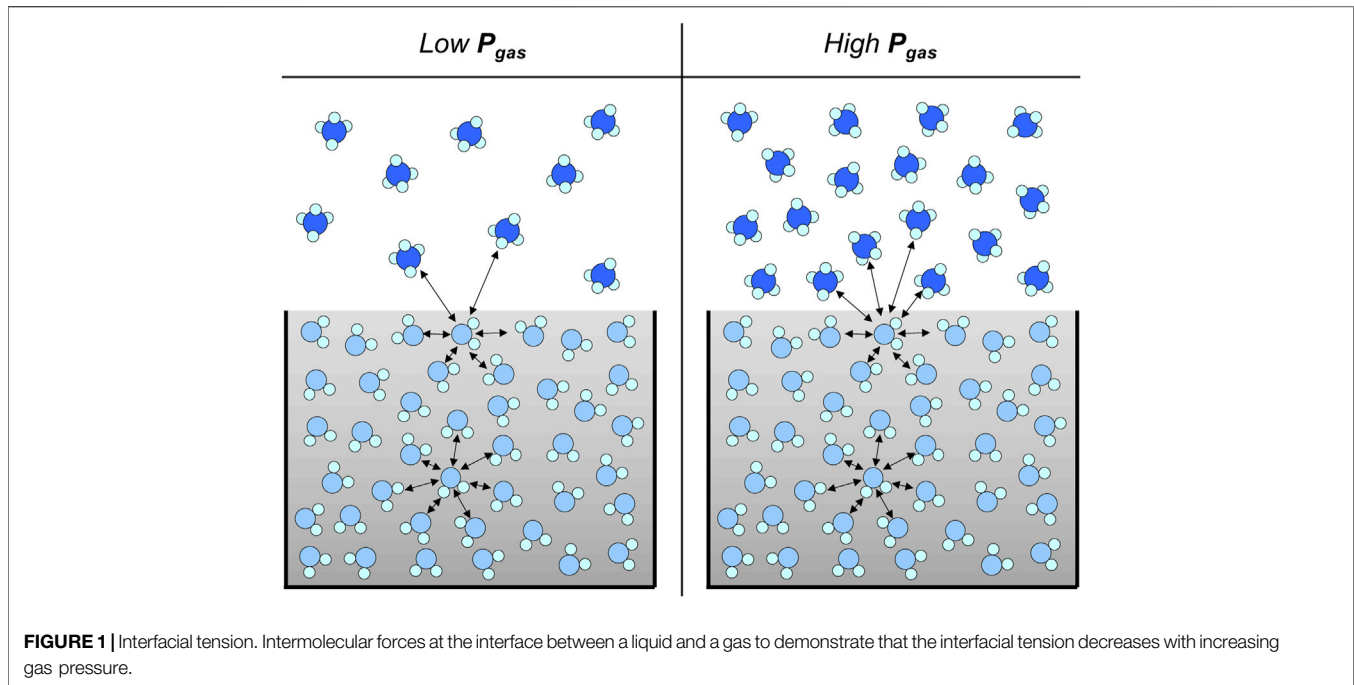
The pore space in sediments is often occupied by more than one fluid. Multi-phase fluids affect unsaturated soil behavior, oil and

gas recovery, energy chemical geostorage, CO₂ geostorage, and the remediation of ground contaminated with light non-aqueous phase liquids (LNAPLs) or dense non-aqueous phase liquids (DNAPLs). The various phases may include gases (air, CH₄, CO₂, H₂, NH₃), liquids (aqueous solutions and organic compounds), and even ice and hydrates.

Fundamental Concepts

Interfacial tension. A molecule at the interface between two fluids experiences different intermolecular forces than the same molecule in the bulk fluid (**Figure 1**). This asymmetry manifests as a surface tension between the phases. Dissolved salts, surfactants, and suspended colloids affect the surface tension; the Gibbs adsorption isotherm relates the interfacial tension under thermodynamic equilibrium γ to the surface excess concentration Γ of the chemical species in the fluid relative to their bulk concentration C_b (Gibbs, 1878). Dissolved CaCl₂ and NaCl have a negative adsorption $\Gamma < 0$ and the interfacial tension increases with salt concentration (Al-Sabhaf et al., 2005; Bachu and Bennion, 2009); on the other hand, some components such as amphiphilic surfactant molecules tend to migrate towards the interface, i.e., positive adsorption $\Gamma > 0$, and the interfacial tension decreases with concentration until surfactants in the bulk solution form micelles when C_b exceeds the critical micelle concentration CMC (Mulligan et al., 2001).

Fluid interfaces contract and extend as they traverse the converging-diverging pore geometry in soils. Thus, we should consider the transient state of the interface instead of the equilibrium state in the analysis of multi-phase fluid flow (Jang et al., 2016; Liu et al., 2021). Time-dependent



adsorption/desorption of surfactants or colloidal particles (e.g., nanoparticles, bacteria, and asphaltenes) controls interfacial tension during interface expansion and contraction. The Langmuir model provides the simplest description of adsorption and desorption kinetics (Langmuir, 1918; Chang and Franses, 1992; He et al., 2015). The adsorption energy increases with particle size; therefore, particles larger than >10 nm tend to experience irreversible adsorption into the interface in contrast to surfactants (Hua et al., 2016). **Figure 2** shows the interfacial tension hysteresis loop of a surfactant solution and a nanofluid droplet in a decane bath (silica nanoparticles: $d = 76$ nm; surfactant: CTAB). Surfactant-coated interfaces exhibit higher hysteresis compared to particle-coated interfaces; in both cases, the interfacial tension increases during rapid droplet expansion.

Contact angle. Young's equation predicts the contact angle θ from force-equilibrium between the interfacial tensions that

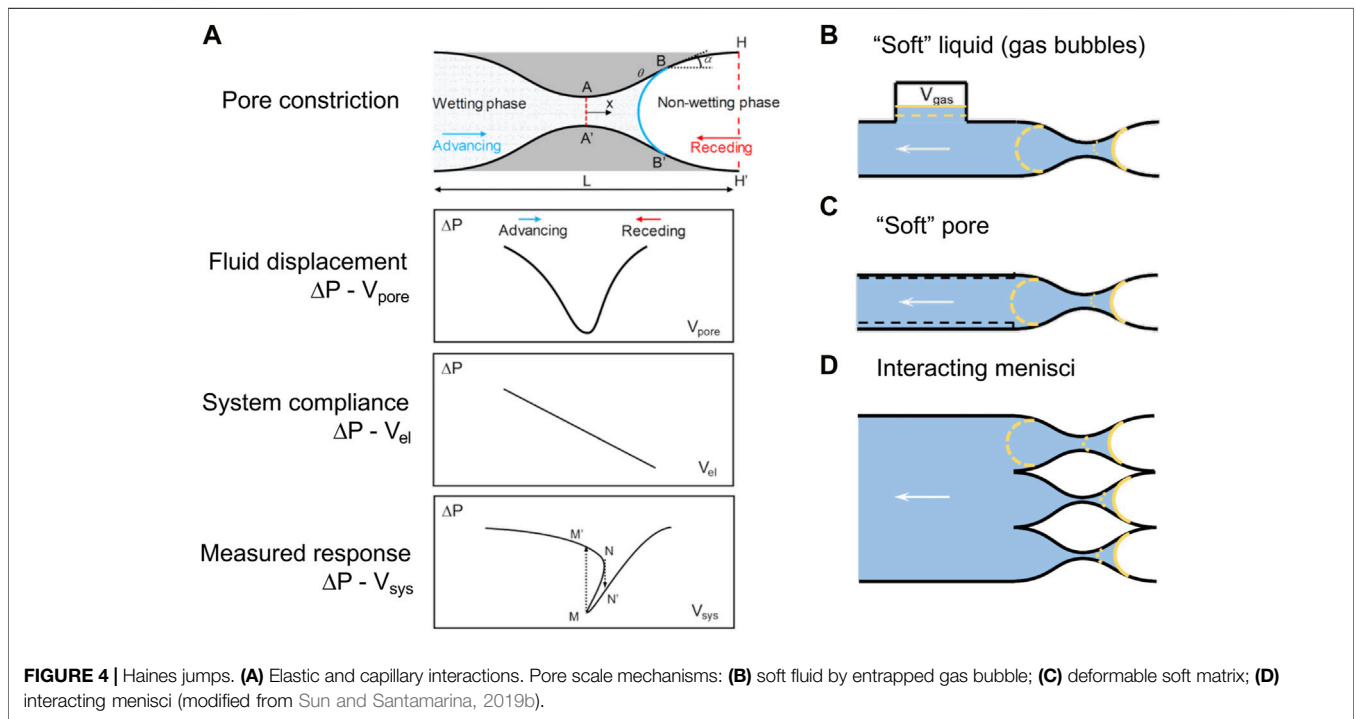
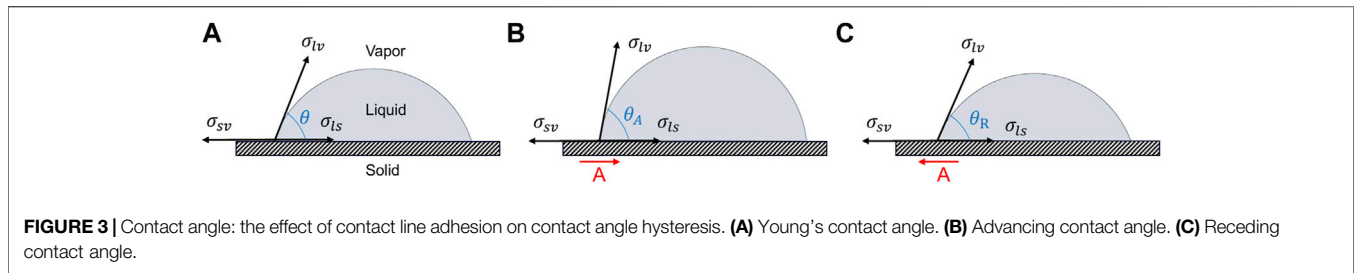
emerge at the fluid–liquid γ_{LV} , liquid–solid γ_{LS} , and fluid–solid γ_{VS} interfaces (**Figure 3A**, Young, 1805):

$$\cos \theta = \frac{\gamma_{VS} - \gamma_{LS}}{\gamma_{LV}}$$

In contrast to the single thermodynamic contact angle predicted by Young's equation, interfaces can exhibit a range of contact angles between two asymptotic values: the advancing contact angle θ_A and the receding contact angle θ_R . Contact angle hysteresis results from surface roughness, chemical inhomogeneities in the solid surface, and solutes in the liquid (de Gennes, 1985; Eral et al., 2013).

The three phases, L–V–S, meet at the contact line. The contact line adhesion A acts against the intended motion and it can be estimated from the advancing and receding contact angles (**Figures 3B,C**):

$$\gamma_{LV} \cos \theta_a + A = \gamma_{VS} - \gamma_{LS}$$



$$\gamma_{LV} \cos \theta_r - A = \gamma_{VS} - \gamma_{LS}$$

$$\Delta u(x) = u_w - u_n = -\frac{4\gamma \cos[\theta - \alpha(x)]}{d(x)}$$

The experimentally measured lateral adhesion force between a liquid droplet and a solid shows the maximum static adhesion followed by a reduced kinetic adhesion, which is remarkably analogous to solid-solid friction (Gao et al., 2018). Surfactants and particles adsorbed at the interface result in complex interface-substrate interaction which alters the contact line pinning.

Non-convex displacement-dependent capillary pressure. The varying pore geometry along the invasion path, transient contact angle behavior, and hysteretic interfacial tension result in non-convex capillary pressure vs. displacement signatures.

1) *Varying pore-geometry along the invasion path.* Consider the displacement of a wetting liquid by a non-wetting fluid across a pore constriction with a sinusoidal geometry as illustrated in **Figure 4A** (viscosity and gravity effects are negligible for small capillary and Bond numbers). The pressure difference between the wetting and the non-wetting fluids $\Delta u(x)$ at position x is a function of the surface tension γ , the contact angle θ and the local pore wall angle $\alpha(x)$:

where $d(x)$ is the pore diameter at position x . The computed capillary pressure for a sinusoidal pore (of circular cross section) shows that the interface experiences a concave-to-convex transition and the capillary pressure reverses sign when the argument $[\theta - \alpha(x)]$ crosses 90° .

- 2) *Contact line pinning and sliding.* Typically, the contact line remains pinned onto the pore wall until it reaches the asymptotic contact angle; thereafter, the contact line slides and the advancing contact angle remains constant (**Figure 5A**). For nanoparticle coated fluid interfaces, they may reach a peak contact angle followed by a pronounced post-peak relaxation to a lower contact angle during steady displacement (**Figures 5B,C**).
- 3) *Buckling of nanoparticle coated interfaces.* The particle surface coverage increases as the interface area decreases across a pore constriction; eventually, a particle shell forms and interfacial tension reverses to compression (Liu et al., 2021). At some

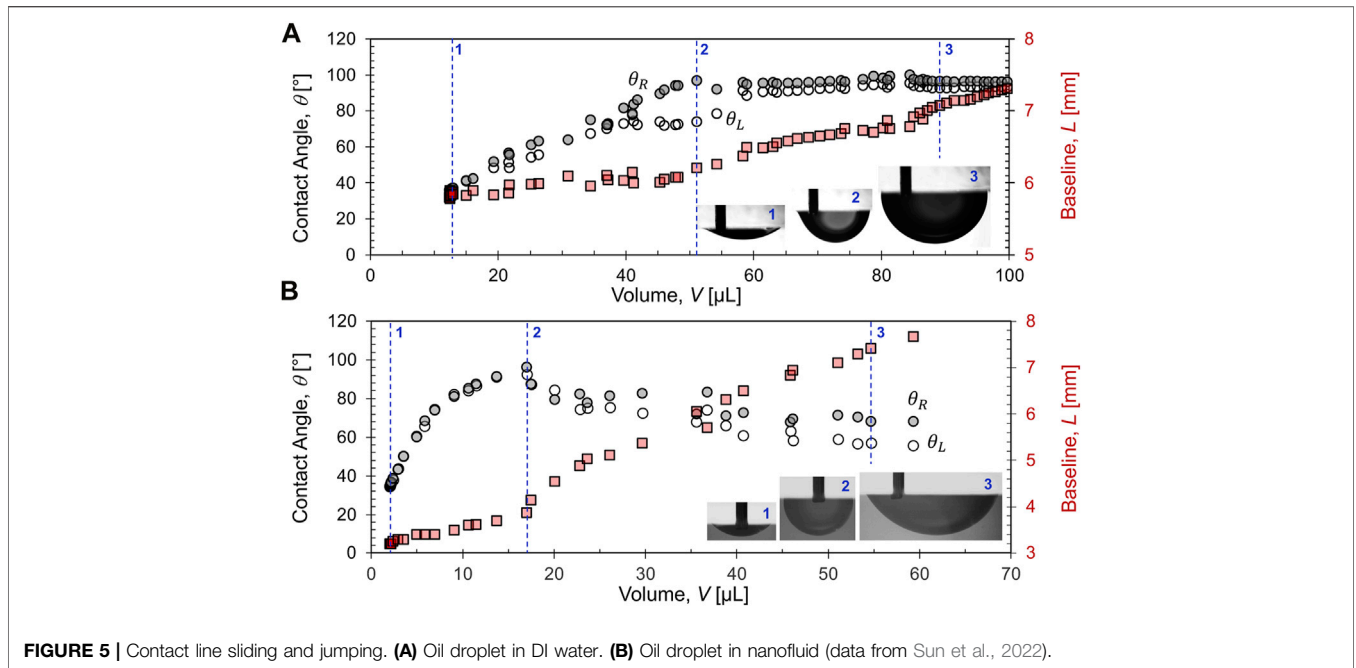


FIGURE 5 | Contact line sliding and jumping. **(A)** Oil droplet in DI water. **(B)** Oil droplet in nanofluid (data from Sun et al., 2022).

point, the shell may buckle or crumple. The buckling resistance is determined by particle-particle and particle-interface interactions. And boundary conditions affect buckling patterns (Meyer et al., 2006; Liu et al., 2021).

Soft-system response \rightarrow Instabilities (Haines jumps and snap-offs). The system deforms in response to changes in capillary pressure. Common causes for a soft system response include 1) the presence of entrapped gas, 2) interacting menisci, and 3) a deformable solid matrix (Figure 4—Note: a deformable solid matrix implies mechanical coupling with the mineral skeleton). Then, displacement-dependent capillarity couples with pressure-dependent volume change to cause “jump” instabilities similar to frictional stick-slip (Sun and Santamarina, 2019b). The sudden local jump of the fluid interface—often known as a Haines jump—causes a transient pressure change and fluid redistribution (Morrow and Szabo, 1970; Gauglitz and Radke, 1989; Berg et al., 2013).

The actual system volume response V_{sys} combines the invaded pore volume V_{pore} with the system’s volume change V_{el} due to a pressure change:

$$V_{sys} = V_{pore} - V_{el}.$$

A jump will occur during either advancing or receding when the resultant ΔP -vs- V_{sys} curve is multivalued, for example, across the pore throat (Sun and Santamarina, 2019b). Then, the potential for instabilities will relate to the pressure required for a volumetric compression $\sim r^3$ given the system stiffness k (Pa/m³) and the capillarity pressure that can arise at the pore constriction of radius r ; in dimensionless form:

$$N_{ec} \propto \frac{K r^4}{\gamma \cos(\theta)}.$$

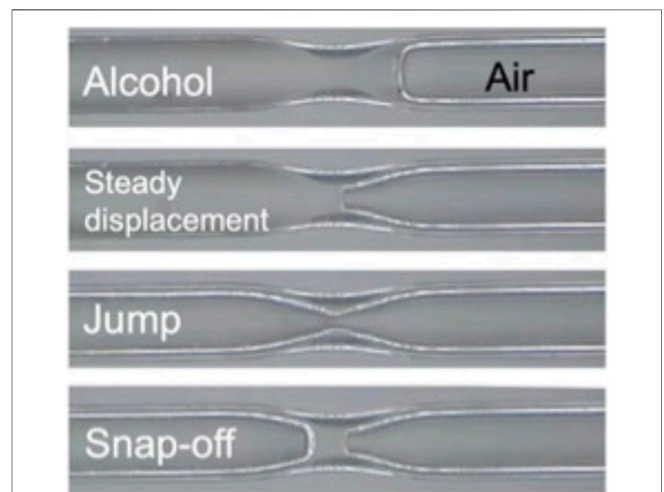
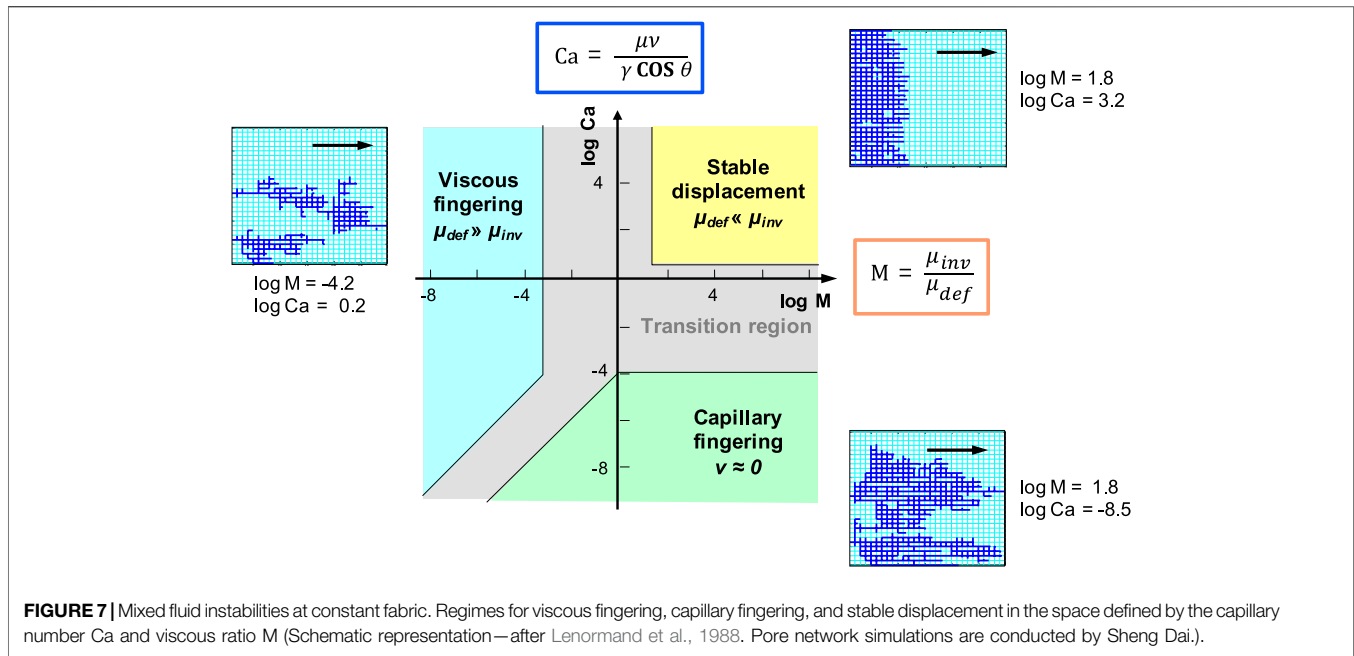


FIGURE 6 | Changes in pore geometry along the advancing path: jumps and snap-offs (Jang et al., 2016).

A system with an elastocapillary number $N_{ec} < 1$ is prone to Haines instabilities.

Wetting fluids transported along corners and crevices or left behind during sudden jumps, i.e., “snap-off,” may accumulate at pore throats to form plugs that split the traversing non-wetting fluid (Figure 6). Snap-offs and plugs result in foam generation inside the porous medium (Lenormand et al., 1983; Peña et al., 2009).



Viscous and capillary fingers. Immiscible fluid displacement is controlled by capillary force F_C , viscous force F_D , and the buoyant force F_b . Critical dimensionless numbers are the capillary number, the viscous ratio and the Bond number (Chatzis and Morrow, 1984; Lenormand et al., 1988; Dawson and Roberts, 1997; Ferer et al., 2004; Santamarina and Jang, 2011; Zhao et al., 2016; see Zhao et al., 2019 for pore-scale modeling methods):

$$\text{Capillary number : } Ca = \frac{\mu v}{\gamma \cos \theta},$$

$$\text{Viscous ratio : } M = \frac{\mu_{inv}}{\mu_{def}},$$

$$\text{Bond number : } Bo = \frac{\Delta \rho g L^2}{\gamma}.$$

Patterns observed during immiscible fluid invasion (i.e., non-wetting) fall into domains defined by these dimensionless numbers: stable displacement takes place at large M and Ca ; viscous fingering at small M and large Ca ; and capillary fingering at large M and small Ca (Figure 7). The Rayleigh-Taylor instability, observed when a lighter fluid ascends through a heavier fluid, develops at large Bond numbers. Different invasion modes lead to distinct fluid pressure fields: the pressure drop occurs mainly in the more viscous phase, i.e., the invading phase in stable displacement or the defending phase in viscous fingering; on the other hand, the viscous pressure drop is negligible compared to the capillary pressure difference between the fluids in the capillary fingering regime (An et al., 2020).

Viscous fingering can also occur in a single phase fluid due to thermal effects, such as during the injection of a hot liquid (low viscosity) into a porous medium saturated with the same liquid at low temperature (higher viscosity). Note: invasion regularizes as

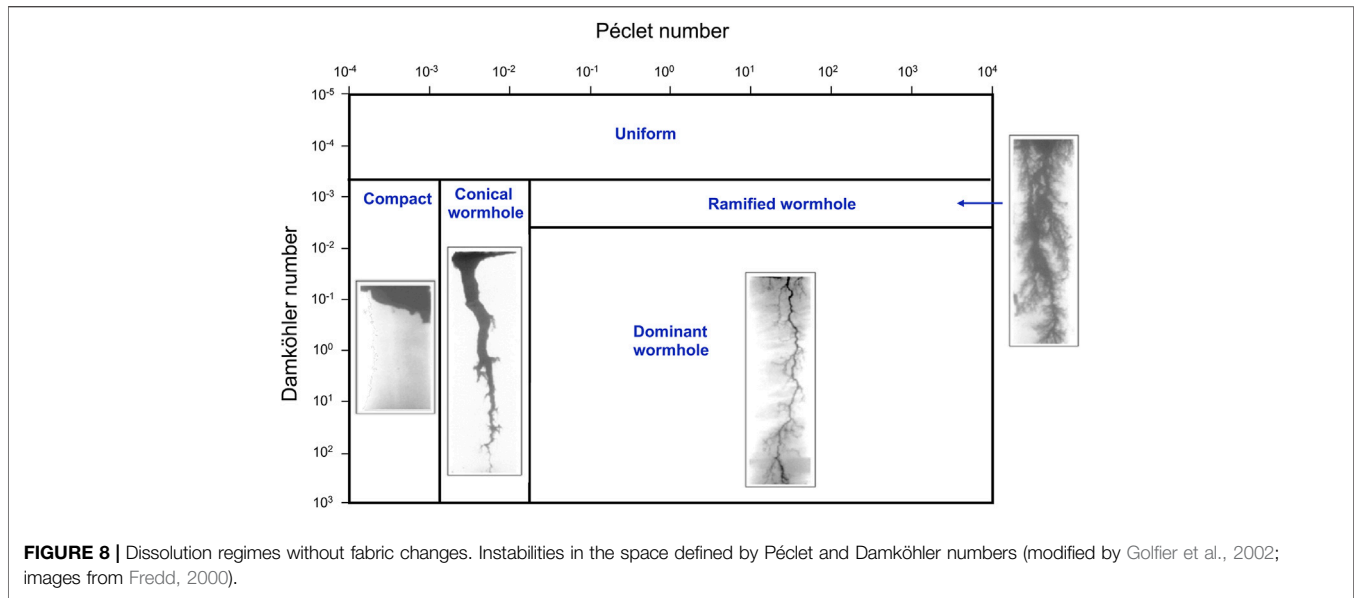
temperature homogenizes) (Helfrich, 1995; Islam and Azaiez, 2010). Thermal viscous fingering may be accompanied by convective currents triggered by the fluid's thermal expansion and density changes.

2.2 Reactive Fluids

Inherent pore size variability results in preferential flow pathways across sediments; in fact, as few as 10% of pores may be responsible for more than 50% of the total flow rate (Jang et al., 2011). Note: Flow channeling is even more pronounced in fractures and fractured rock masses (National Academies of Sciences, Engineering, and Medicine, 2020; Cardona et al., 2021). These preferential flow paths will also deliver the majority of the reactants to cause either dissolution or precipitation within the soil mass.

Precipitation is a self-homogenizing process: it reduces transport along preferential flow paths and reactive fluids deviate to other pathways. On the other hand, dissolution tends to localize due to positive feedback; preferential flow channels enlarge and lead to increased flow focusing and “wormhole” formation (Menke et al., 2017; Derr et al., 2020). Wormholes affect dam stability (Romanov et al., 2003), CO_2 sequestration (Kim and Santamarina, 2015), groundwater transport in karst terrain (Dreybrodt, 1990), and acid stimulation of oil reservoirs (Fredd and Scott Fogler, 1998; Al-Arji et al., 2021). In the absence of advection, diffusive reactant transport promotes homogeneous dissolution.

The previous discussion suggests that dissolution topologies in rigid porous media such as in rocks depend on three concurrent processes: diffusion, advection, and chemical reaction. Two dimensionless ratios combine the three time scales for advection t_{adv} , diffusion t_{diff} , and reaction t_r for a channel length L_{ch} :



$$\text{Damköhler number } Da = \frac{t_{adv}}{t_r} \propto \frac{kL_{ch}}{v},$$

$$\text{Péclet number } Pe = \frac{t_{diff}}{t_{adv}} \propto \frac{vL_{ch}}{D},$$

where the process parameters are the kinetic rate of the reaction k [1/s], the average pore velocity v [m/s] and the diffusion coefficient D [m²/s]. The Pe-Da diagram in **Figure 8** captures the space for the various dissolution topologies: compact dissolution, conical wormhole, dominant wormhole, ramified wormhole, and uniform dissolution regimes. Low advection velocities—long t_{adv} and small Pe—allow reactant consumption near the inlet and instabilities cannot develop; conversely, very high advection velocities—short t_{adv} , high Pe and small Da—carry reactants throughout the porous medium from inlet to outlet and favors a stable homogeneous dissolution. Wormholes develop with intermediate flow rates—large Da and Pe—so that reactants act preferentially along flow channels. Finally, we note that extensive dissolution in granular materials will cause fabric changes, as discussed later in this manuscript.

2.3 Particle-Laden Fluids

Particle-laden fluids are common in nature (e.g., ground water flow) and frequently used in engineered applications (tremie submerged construction, drilling muds, and well stimulation and proppants).

Particle inclusion changes the liquid density, rheology, and interfacial properties. Density triggers convective fingers in water columns, as seen during the release of mine waste slurries in large water bodies (Rayleigh-Taylor instability; Lange et al., 1998; Völtz et al., 2002).

The suspension viscosity increases with a higher mineral volume fraction and more frequent inter-particle interactions result in fluids with yield stress; then, instabilities readily emerge. For example, air injection into dense granular suspensions results

in bubble migration with frictional stick-slip characteristics and viscous fingering (Sandnes et al., 2011).

A particle embedded in a moving fluid experiences buoyant weight F_B , drag F_D , inertia against motion changes F_I , and electrical interaction with pore walls F_{wall} (it combines van der Waals and electrostatic forces, including hydrophobic adhesion forces). These forces combine to produce self-stabilizing clogging rings in convergent radial flow (negative feedback during fluid extraction), and fingered erosion during outward fluid flow (positive feedback during fluid injection) (Valdes and Santamarina, 2006; Valdes and Carlos Santamarina, 2007; Liu et al., 2019). The dimensionless ratios between interacting forces define the various particle migration regimes in terms of the particle size d , obstacle size D , particle and fluid mass densities ρ_p and ρ_f , fluid viscosity μ , fluid velocity v , and gravity g :

$$\text{Contact number} = \frac{\text{Wall interaction}}{\text{Drag}}$$

$$N_{ad} = \frac{F_{wall}}{F_D} \propto \frac{F_{wall}}{\mu d v},$$

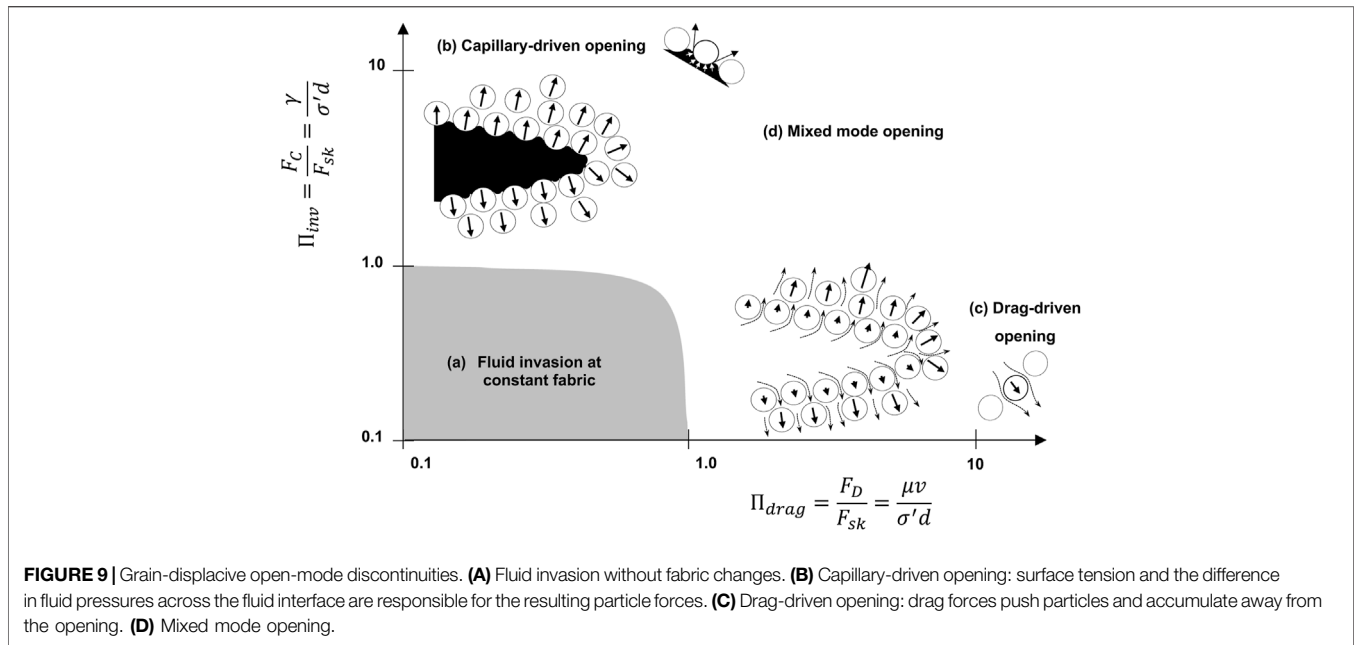
$$\text{Archimedes number} = \frac{\text{Buoyant weight}}{\text{Drag}}$$

$$Ar = \frac{F_B}{F_D} \propto \frac{g d^2 (\rho_p - \rho_f)}{\mu v},$$

$$\text{Stokes number} = \frac{\text{Inertia}}{\text{Drag}}$$

$$\text{Stk} = \frac{F_I}{F_D} \propto \frac{\rho_p d^2 v}{\mu D}.$$

Clogged pore constrictions alter flow in nearby open paths, affect retardation, and may promote neighboring clogging. Experimental observations show that the probability of neighboring clogging is much higher than the probability of independent clogging (Liot et al., 2018; Van Zwieten et al., 2018; Liu et al., 2019).



Under mixed-phase conditions, particle-laden fluids may experience preferential particle accumulation at the interface with other immiscible fluids, e.g., hydrophobic nanoparticles suspended in water. This situation may stabilize interfaces and hinder coalescence (e.g., Pickering emulsions) or prompt pore-scale interfacial instabilities such as interface buckling and the stick-slip response of the contact line, as reviewed earlier. Under radial flow conditions (fluid injection), particle bands develop away from the injection point due to gravity and inertia; additional injection can break the particle bands and form erosion fingers (Kim et al., 2017).

3 FLUID-DRIVEN INSTABILITIES WITH FABRIC CHANGES

Pressure gradients, capillarity, mineral dissolution, and various forms of flow localization in rigid porous media may collude with the granular nature of soils and sediments to give rise to mechanically coupled instabilities that cause fabric changes. At the macroscale, mechanical coupling implies changes in effective stress. At the particle scale, these instabilities reflect the interplay between particle level forces. The following sections analyze fluid-driven instabilities with fabric changes and the underlying forces; given the wide range of possible interactions, the list is limited to frequently encountered field conditions.

3.1 Single-Phase Fluid—Miscible Invasion

The effective stress principle $\sigma' = \sigma - u$ anticipates a gradient in effective stress when there is a fluid pressure gradient $d\sigma'/dx = -du/dx$. At the particle level, the flowing fluid gradually transfers its pressure as viscous drag onto the particles; hence, pressure decreases and interparticle skeletal forces accumulate in the direction of fluid flow. Then, the *ab initio* formation of a

fluid-driven open mode discontinuity involves the following sequence of events: fluid injection at a point causes radial fluid flow; drag forces push particles away from the injection point, i.e., cavity expansion; tangential extension and the particles' relative displacement result in a surface imperfection that facilitates preferential fluid flow; arising tangential drag forces cause further interparticle separation (**Figure 9C**). The positive feedback built into this sequence of events leads to the development of open-mode discontinuities, including planar “hydraulic fractures” (Shin and Santamarina, 2010; 2011b; Carrillo and Bourg, 2021) as well as tubular pipes (Cartwright and Santamarina, 2015). Note: the term “open-mode discontinuity” is preferred instead of “fracture” in the context of granular materials, i.e., without cohesion; moreover, models that are based on classical fracture mechanics are inadequate for the analysis of open mode discontinuities in granular materials.

Particles experience two forces in single-phase fluid flow (without changes in pore fluid chemistry): the skeletal force F_{Sk} and the drag force F_D . The associated dimensionless ratio is

$$\Pi_{drag} = \frac{F_D}{F_{Sk}} \propto \frac{\mu v}{\sigma' d}$$

Therefore, high invasion velocity v , low effective stress σ' and small grain size d favor the development of drag-driven open-mode discontinuities.

Earthquakes are natural triggers of fluid-driven localizations. When saturated loose sands liquefy during an earthquake, the liquefied layer typically forms at a depth $5 \text{ m} < z < 20 \text{ m}$, i.e., sufficiently deep to be contractive but shallow enough so that the dynamic strain exceeds the elastic threshold strain (Ishihara, 1993; 1997). During liquefaction, the effective stress vanishes and the pore fluid pressure reaches the overburden stress (Ishihara, 1993; Lee and Santamarina, 2007). The excess pore pressure may gradually drain through the upper unliquefied layer

or trigger a vertical open-mode discontinuity for rapid drainage; in fact, the aligned sand boils often observed on grassy fields reveal the underlying open discontinuity that links the liquefied layer to the surface (Chameau et al., 1991; Bardet and Kapuskar, 1993; Schneider and Mayne, 2000; Sukkarak et al., 2021).

3.2 Multi-Phase Fluids—Immiscible Invasion

Immiscible fluids experience capillarity in the pore space of granular materials, and the wetting fluid is at a lower pressure than the non-wetting fluid, $\Delta u = u_n - u_w$. The granular skeleton picks up the pressure difference in terms of a change in effective stress (hence, Bishop's model). At the particle scale, the capillary force acting on a particle $F_C = \pi d \cdot \gamma$ can significantly alter the preexisting effective stress dependent particle forces $F_{sk} = \sigma' d^2$, where d is the particle diameter and γ the interfacial tension. The ratio between these two forces

$$\Pi_{inv} = \frac{F_C}{F_{sk}} \propto \frac{\gamma}{\sigma' d}$$

defines two distinct invasion regimes (Figure 9 - Shin and Santamarina, 2011b; see also Holtzman et al., 2012; Carrillo and Bourg, 2021):

- 1) pore-invasive $\Pi_{inv} = \gamma/(\sigma' d) \ll 1$: the non-wetting phase travels from pore-to-pore across pore throats without disturbing the granular skeleton.
- 2) grain-displacive $\Pi_{inv} = \gamma/(\sigma' d) \gg 1$: the capillary pressure displaces sediment grains away from the invading phase.

In general, invasion is grain-displacive in fine-grained sediments at low effective stress. Still, other forms of mixed-fluid instabilities can take place in coarse-grained sediments, but these are mechanically decoupled from the granular skeleton (refer to "fluid-driven instabilities at constant fabric" described in the previous section).

The concepts of interfacial tension, contact angle, and capillary pressure explored earlier for immiscible fluids can be extended to analyze other systems, including water-ice (i.e., frozen ground engineering) and water-hydrates (i.e., hydrates bearing sediments). Often, the immiscible fluid invades the boundary and remains as a continuous phase. However, ice, hydrate, and gas bubbles, may nucleate inside the porous. Examples of gas nucleation include exsolution during depressurization (e.g., sampling marine sediments), water cavitation (e.g., rapid shear induced dilation under undrained conditions), or heat-induced phase transformation. Boundary invasion or internal nucleation may result in the same degree of saturation, yet there are salient differences in other macroscale physical properties such as the capillarity pressure vs. degree of saturation, relative permeabilities, bulk stiffness, consolidation, and shear strength (Sills et al., 1991; Rebata-Landa and Santamarina, 2012; Jang and Santamarina, 2014).

Desiccation cracks: non-wetting air invasion into a water-saturated sediment. Consider a clay bed sedimented from a slurry. The supernatant water evaporates until the air-water

interface reaches the sediment surface. Further evaporation requires the interface to go down, but the air-water clings onto the water-wet mineral grains, dragging them down (internally, the water experiences suction and the effective stress increases). Eventually, the sediment will resist further compaction, and additional suction causes the air-water interface to invade the sediment, starting at the largest pores (often associated with surface defects). At the invaded defect, suction causes particle displacement normal to and away from the air-water interface. Thus particles displace away from each other at the tip, further air invasion takes place, and eventually forms a desiccation crack (Figures 10A,B; Shin and Santamarina, 2011b; 2011a; Cordero et al., 2017). Desiccation cracks may also nucleate and grow within the sediment, i.e., beneath the surface, when suction triggers gas exsolution or cavitation within the sediment (Figure 10C - Zhao and Santamarina, 2020).

Non-wetting buoyant fluid columns. Buoyant oil or gas with a density ρ_b may mobilize long column heights H ; then, the capillary pressure at the top of the column is $\Delta u = H \cdot (\rho_w - \rho_b)g$. In agreement with the aforementioned discussion, the buoyant column may migrate upwards by pore-invasion or it may cause grain-displacement and propagate an open-mode discontinuity. We captured high-resolution grain-displacive gas invasion patterns by injecting air into transparent sediments subjected to controlled effective stress (see Sun and Santamarina, 2019a for details). Gas ascends as bubbles at very low effective stress and high Π_{inv} (Figure 11A). At intermediate effective stresses, the gas inclusion starts growing as a succession of cavity expansion events (Figures 11B, B); gradually, the cavity develops corners and edges; local fractures initiate at high curvature zones and eventually grow to form either one or two thin circular planar openings, or "fractures" (Figures 11B,C). Gases expand as the water pressure decreases during ascension and often form pockmarks when they reach the seafloor.

Non-wetting ice and hydrate growth in sediments - The local effective stress. Ice and hydrates require the proper pressure and temperature conditions for phase stability; in addition, hydrate formation is typically gas-limited. When appropriate, both ice and hydrate nucleate on mineral surfaces (heterogeneous nucleation) and grow into the pore space until they reach the surrounding pore walls. Further growth of the non-wetting ice or hydrate phases is either pore invasive $\Pi_{inv} = \gamma/(\sigma' d) \ll 1$ or grain displacive $\Pi_{inv} = \gamma/(\sigma' d) \gg 1$. Hydrate or ice lenses and veins result from grain displacive formation (Dai et al., 2012; Lei and Santamarina, 2018). Tomographic images in Figure 12 show various ice topologies in different sediments: 1) the sand specimen shows no ice lenses (pore-invasive ice growth); 2) the bentonite specimen is massively crisscrossed by ice lenses (grain-displacive); 3) the onion-like lens structure that develops in the high water content kaolinite specimen reflects the interplay among ice formation, stress changes, and the evolving sediment compaction with cryo-suction; thus, there are no ice lenses in the core.

The onion-like topology of ice lenses in Figure 12C suggests that the growth of grain-displacive instabilities reflects the evolving local effective stress. To test this hypothesis, we

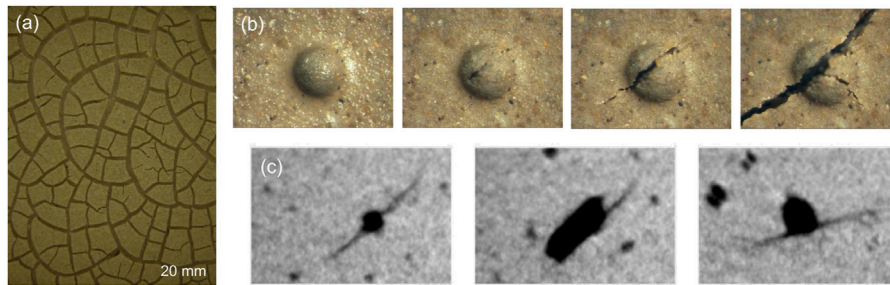


FIGURE 10 | Grain-displacive non-wetting fluid invasion: desiccation cracks. **(A)** Surface desiccation cracks (Shin and Santamarina, 2011b). **(B)** Crack initiation at a surface defect during drying (Shin and Santamarina, 2011a). **(C)** Internal desiccation cracks observed using X-ray micro CT (Zhao and Santamarina, 2020).

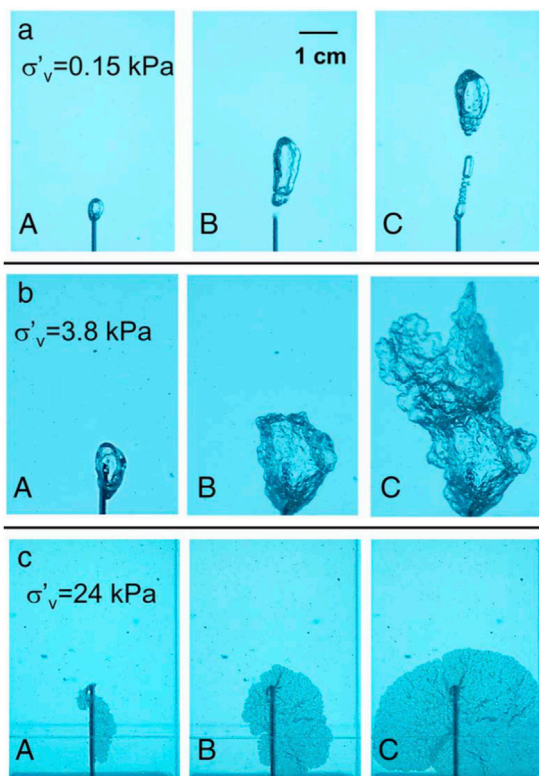


FIGURE 11 | Grain-displacive gas migration in a transparent fine-grained granular medium at different vertical effective stress levels: **(A)** bubble at $\sigma'_v = 0.15$ kPa; **(B)** cavity expansion followed by planar opening at $\sigma'_v = 3.8$ kPa; and **(C)** open discontinuity at $\sigma'_v = 24$ kPa (Sun and Santamarina, 2019a).

prepared cylindrical disk specimens using water saturated kaolinite paste; after consolidation to $\sigma'_z = 30$ kPa in cylindrical oedometers, the 10 cm diameter and 7 cm thick specimens were extruded from the k_o cell and a radial V-shaped slice was cut and removed from each specimen. Then, we imposed tension at the center of some specimens by pulling the groove walls apart (200 g weights), and compression by sitting other specimens on lateral supports (Yun, 2005). In all tension cases, an ice lens formed and propagated vertically from the groove tip following the tensile

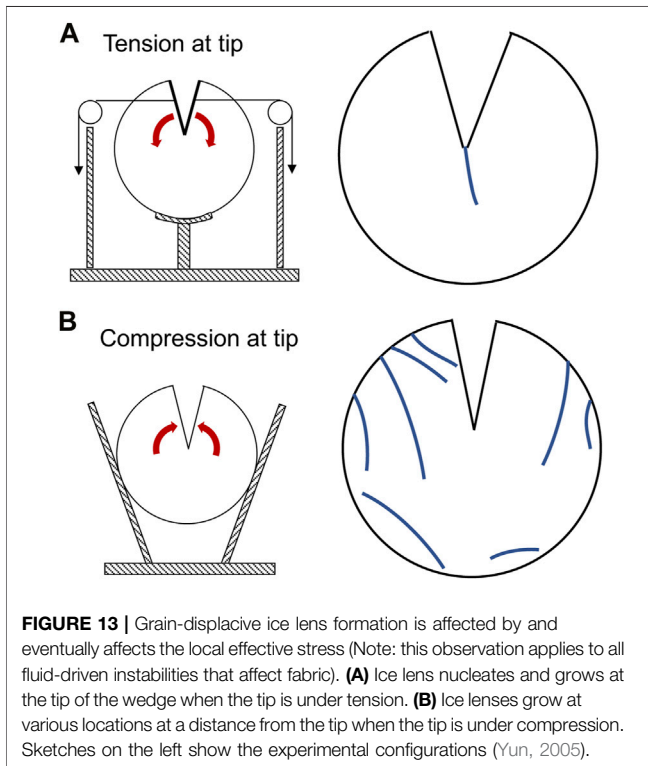
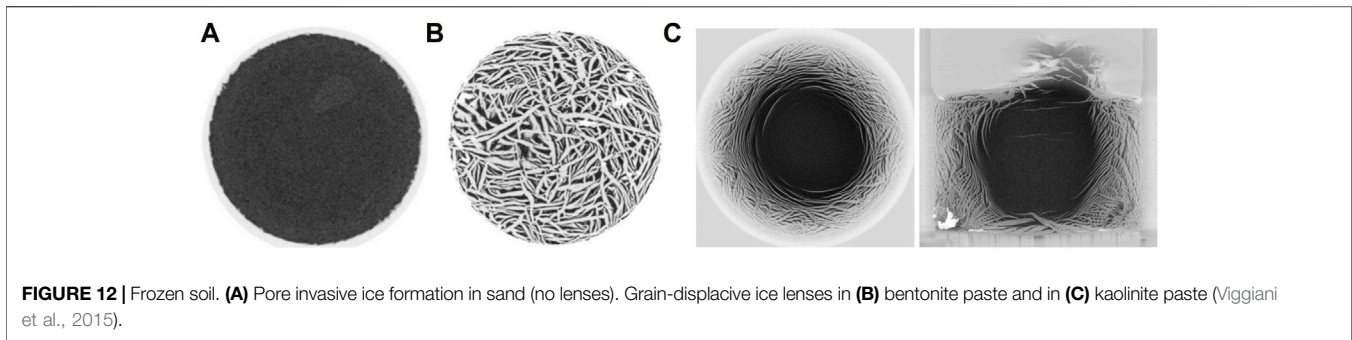
field (**Figure 13A**). In contrast, lenses did not form at the center when the groove tip was under compression (**Figure 13B**). These results and the onion-shaped topology of ice lenses in **Figure 12** confirm that the growth of mechanically-coupled grain-displacive instabilities responds to and alters the local effective stress field (Note: this observation applies to all instabilities discussed in this section).

Wetting fluid imbibition: capillary contraction. Spontaneous water imbibition into a dry or partially saturated hydrophilic soil tends to cause volume contraction as capillary forces pull particles towards the invading water front. Potential instabilities include peripheral open-mode discontinuities surrounding the area subjected to wetting, and pronounced volume collapse (e.g., collapsible loess—combines cementation dissolution and loss of suction at interparticle contacts—Barden, McGown and Collins, 1973; Houston et al., 1988; Rinaldi et al., 2001; Lourenco et al., 2012; Bruchon et al., 2013; Li et al., 2016). On the other hand, partially saturated, dense soils and soils with swelling minerals may swell when water content increases (Berney, 2004).

3.3 Reactive Fluid Flow

Reactive fluids traverse the granular medium, causing either mineral dissolution or precipitation. Precipitation is self-homogenizing because transmissivity decreases more rapidly along the more conductive pathways (i.e., negative feedback); overall, precipitation produces a marked increase in stiffness, dilative tendency, and strength (by either adding cohesion or increasing the friction angle—Jung et al., 2012).

On the other hand, post-depositional dissolution is significantly more complex. Initially, dissolution evolves as predicted in the dimensionless Pe-Da space for rigid porous media (**Figure 8**). Rather than wormhole formation (limited by arching instability), grain dissolution readily affects interparticle coordination and forces, triggers fabric rearrangement, and the void ratio evolves towards a stress-dependent terminal value closer to e_{\max} . Consequently, both hydraulic and mechanical properties are affected; in particular, there is an increased contractive tendency (Cha and Santamarina, 2014). Furthermore, experimental and discrete element DEM simulation results show that 1) the horizontal stress ratio k_o decreases during dissolution and it can reach the active value k_a (i.e., internal shear failure), often followed



by horizontal stress recovery; 2) the anisotropy in coordination reaches a maximum as the stress ratio approaches k_d , and 3) there is a marked difference in the internal fabric between the initial and post-dissolution conditions even if boundary stresses return to similar values (Shin and Santamarina, 2009; Cha and Santamarina, 2016, 2019a).

Minerals dissolve preferentially at grain contacts under high stress. Solutes diffuse towards the pore space and reprecipitate on unstressed grain surfaces nearby. (Note: this phenomenon is known as pressure solution Weyl, 1959; Rutter, 1983; Etheridge et al., 1984; Fowler and Yang, 1999; Croizé et al., 2010). Pressure-dependent mineral dissolution adds additional complexity: strong force chains in the granular skeleton collude with force-dependent dissolution to create the positive feedback dissolution that promotes the emergence of shear localization as the stress ratio (or force anisotropy) reaches failure conditions under zero lateral strain and constant vertical stress boundary conditions (Cha and Santamarina, 2019b). In the

shear band, the porosity is higher and the coordination number is lower than in the surrounding soil mass, strong force chains form and grains experience faster dissolution (Figure 14). Shear discontinuities triggered by mineral dissolution may explain the non-tectonic origin of polygonal faults observed in marine sediments and lacustrine deposits (Cartwright and Dewhurst, 1998; Shin et al., 2008).

3.4 Particle-Laden Fluids

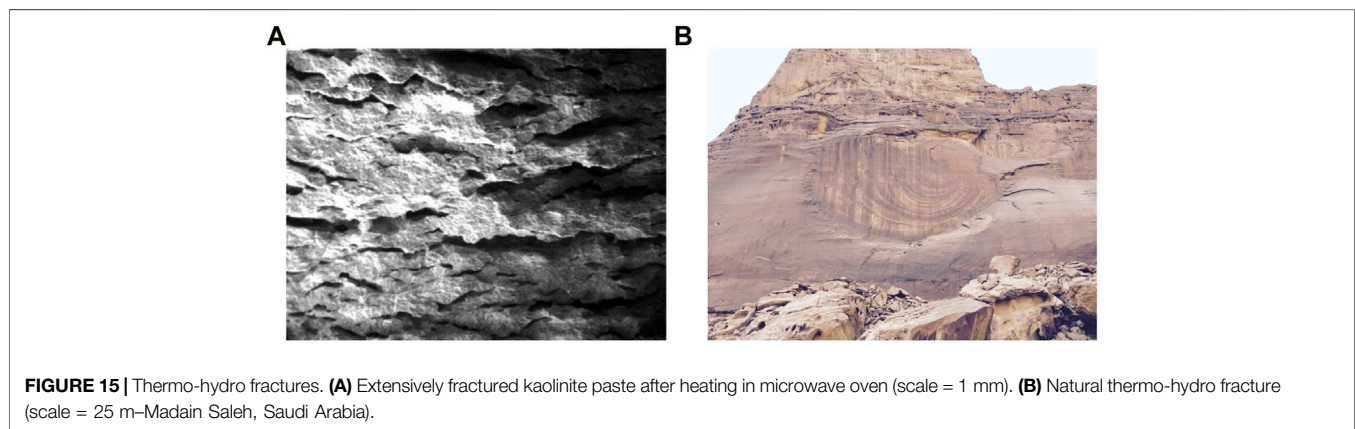
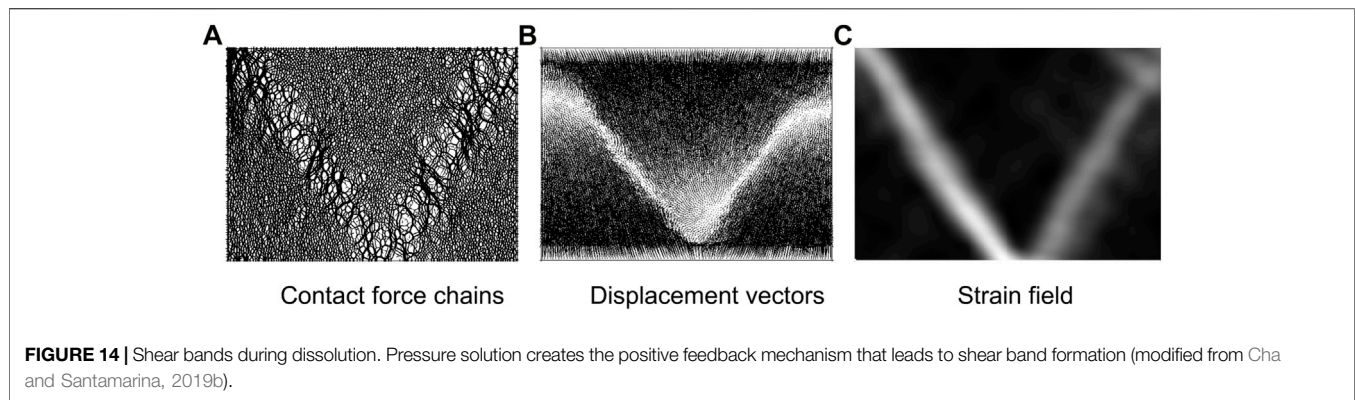
Flowing fluids can remove and drag grains away. Particle deposition takes place downstream as the flow velocity decreases and its carrying capacity diminishes. The geological record has extensive evidence of sediment erosion-and-deposition phenomena, including: cm-scale sand boils downstream of eroding dams; km-scale mud volcanoes (e.g., Lusi—Indonesia); pipes; and sand dikes observed in marine seismic sections (Hovland et al., 2002; Chand et al., 2012; Moss et al., 2012).

At low fine content, the overburden load is carried by the skeleton-forming coarse grains, and load-free fine particles can be detached and dragged away (Skempton and Brogan, 1994; Moffat et al., 2011). In this case, particle erosion is accompanied by an increase in hydraulic conductivity but without volume change (Suffusion—Fannin et al., 2015). Soils sensitive to suffusion fall under the GF(F), G(F), G(G), GS(S), S(F), or S(S) groups in the Revised Soil Classification System (See Castro et al., 2022). At the macroscale, the feedback mechanism in suffusion resembles dissolution channeling, yet mass removal takes place as grains rather than dissolved species.

On the other hand, energy-intensive erosion may gradually destabilize the load carrying skeleton, causing significant volumetric contraction and even skeletal collapse (suffosion). Regressive or backward erosion piping is a major concern in dam stability (a potential mechanism behind the Teton dam's failure—Sherard, 1987). It requires long seepage pathways to minimize the gradient at the exit or filters against clay cores to prevent fine migration (Li and Jonathan Fannin, 2008; Chang and Zhang, 2013; Hendron, 2013; Robbins and Van Beek, 2015; Santamarina et al., 2019).

3.5 Instabilities Caused by Other Fluid-Skeleton Couplings

All forms of energy are coupled, including thermal, chemical, hydraulic, and mechanical THCM (Mitchell, 1991). Under the



right boundary conditions, mechanically-coupled processes can eventually cause instabilities in granular media. Two examples follow:

- 1) Thermo-hydro-mechanical THM coupling: thermal water expansion can build up pore pressure and cause a hydraulic fracture if the rate of heating is higher than the rate of pore water pressure dissipation; both are diffusion processes, therefore the ratio $\Pi_{THM} = D_T/c_v$ between the thermal diffusion D_T and pressure diffusion c_v coefficients determines the domain for this localization. For saturated soils, the thermal diffusion coefficient varies between $D_T = 4 \cdot 10^{-7} \text{ m}^2/\text{s}$ for clays to $D_T = 8 \cdot 10^{-7} \text{ m}^2/\text{s}$ for sands, while the coefficient of consolidation can range between $c_v \leq 10^{-8} \text{ m}^2/\text{s}$ for clays to $c_v \geq 10^{-3} \text{ m}^2/\text{s}$ for sands (Márquez et al., 2016). Clearly, Π_{THM} increases for high specific surface soils thus clay-controlled fabrics are prone to thermal fracturing. Given its massive expansion, water-to-steam transformation is particularly detrimental (the expansion ratio is $\sim 1,600$ at atmospheric pressure). **Figure 15** shows two examples of thermal fracturing: a mud ball exposed to microwave heating (**Figure 15A**) and a sedimentary layer subjected to lava flow (**Figure 15B**).
- 2) Chemo-hydro-mechanical CHM coupling: A diffusing salt front causes a pressure front that precedes it. The pressure front can produce a hydraulic fracture, followed by surface

contraction cracks above it (recently observed by Mengwei Liu in our laboratory). These CHM-driven instabilities result from changes in electrical interparticle forces (van der Waals, double layer, osmotic) and may emerge in high specific surface fine-grained clayey sediments. By contrast, the dissolution-based instabilities described earlier apply to coarse-grained sediments such as silts and sands.

4 DISCUSSION

The previous sections identified a wide range of localizations and described the underlying positive feedback mechanisms conducive to instabilities. **Table 2** summarizes the critical dimensionless ratios involved in these processes. In all cases, we focused on pore and particle scale phenomena to analyze the initiation and evolution of instabilities.

Forces. The magnitude of interparticle forces is a function of grain-size; therefore, grain-size plays a central role in defining the space for various instabilities. **Table 3** lists interparticle forces and corresponding equations for first-order estimates. We can see that grain weight F_w , buoyancy and inertia relate to volume $f(d^3)$, the force acting on a grain that is part of a load carrying skeleton F_{sk} scales with its area $f(d^2)$, while drag F_D , capillary F_C , and electrical interactions are proportional to size $f(d)$. These equations define straight lines in log-log plots; therefore, the

TABLE 2 | Pore/particle scale dimensionless ratios that define the domains for fluid-driven instabilities. The selected ratios presented here resemble the analysis in the text.

Instability	Critical dimensionless number	Expression	Physical meaning
Haines jumps	Elastocapillary number N_{ec}	$Nec = Kr^A/\gamma \cos\theta$	Elasticity of the system/ capillary force
Viscous and capillary fingerings	Capillary number Ca	$Ca = \mu v/\gamma \cos\theta$	Viscous force/ capillary force
	Viscosity ratio M	$M = \mu_{inv}/\mu_{def}$	Viscosity ratio between invading and defending fluids
Reactive fluids	Bond number Bo	$Bo = \Delta\rho g L^2/\gamma$	Buoyant force/ capillary force
	Damköhler number Da	$Da = kL_{cf}/V$	Time scale of advection/ reaction
Particle-laden fluids	Péclet number Pe	$Pe = vL_{cf}/D$	Time scale of diffusion/ advection
	Archimedes number Ar	$Ar = gd^2 (\rho_p - \rho_l)/\mu v$	Terminal velocity/ flow velocity
	Stokes number Stk	$Stk = \rho_p d^2 v/\mu D$	Inertia effect
Open-mode discontinuity	Contact number N_{acd}	$N_{acd} = F_w/\mu d v$	Contact force/ drag force
	Capillary invasion number	$\Pi_{inv} = \gamma/\sigma' d$	Capillary force/ skeletal force
Thermo-hydro-mechanical THM coupling	Drag-driven invasion number	$\Pi_{drag} = \mu\gamma/\sigma' d$	Drag force/ skeletal force
	Thermal expansion number	$\Pi_{THM} = D_T/C_v$	Thermal diffusion/ pressure diffusion

TABLE 3 | Particle-level forces. They scale with d , d^{2+} , and d^3 . The ratio between the skeletal force and all other forces confirms the importance of the particle buoyant weight in coarse-grained sediments and of capillary, drag, and electrical forces on phenomena that take place in fine-grained sediments (Mitchell, 1976; Santamarina, 2003).

$\propto d^3$	Weight $F_w = \pi/6 \rho_p m d^3$
	Buoyant $F_U = \pi/6 \rho_l g w d^3$
$\propto d^2$	Skeletal $F_{sk} = \sigma' d^2$
	Thermo-elastic $F_{Th} = \alpha_{sk} \Delta T G_{sk} d^2$
$\propto d$	Capillary $F_C = \pi \gamma_L V d$
	Drag $F_D = 3\pi \mu v d$
	Electron attraction $Att = 0.04 A_p/t^2 d$
	Electron repulsion $Rep = 0.002 \sqrt{C_0} e^{-10^8 t \sqrt{C_0}} d$

different forces intersect at specific particle sizes. For example, self-weight and the capillary force are equal at $d \approx 2$ mm; self-weight prevails for larger particles while capillarity gains relevance for finer soils. Similarly, we can anticipate that electrical interactions gain relevance for high specific surface submicron particles and vanish in silts and sands.

Instability, nucleation, and growth. Scaling analyses and dimensionless ratios hide the intricate physical details at the pore/grain scales that eventually lead to macroscale instabilities. Localizations start at nucleation sites that are typically associated with the inherent variability in granular materials. For example, liquefaction and shear band formation are delayed in homogeneous sands compared to heterogeneous specimens at the same density (Frost et al., 2019). Similarly, desiccation cracks start at surface or subsurface imperfections, or “dimples” (see **Figure 11**), and dissolution wormholes evolve from the preferential conduction paths initially present in the porous network. In fact, numerical simulations that capture natural variability systematically render more “natural” results (e.g., a porosity random field with or without spatial correlation).

After nucleation, positive feedback mechanisms sustain further growth. For example, there are pronounced differences in the interparticle forces around an open-mode discontinuity triggered by viscous forces (hydraulic fracture) and by capillary forces (e.g., desiccation crack or ice lens). Yet, particle forces cause unloading and extension at the opening tip in both cases, which favors water invasion (in hydraulic fractures) and interface

invasion (in desiccation cracks and ice lenses). Therefore, macroscale simulations require particularly sensitive relations between the permeability and void ratio (hydraulic fracture), or the entry pressure and void ratio (in desiccation cracks).

We can extend this discussion to all forms of fluid-driven granular instabilities; analysis and simulations must capture the governing conditions in terms of dimensionless ratios, recognize the local pore and grain-scale processes, identify the source of positive feedback, and select constitutive relations with high sensitivity to local changes.

Local vs. global instabilities. The evolution of local instabilities may cease and not evolve into large scale instabilities. For example, 1) the contact line displacement for a liquid advancing on a flat surface consists of numerous local stick-slip events, yet the macro-scale movement and front geometry may appear smooth (high frequency jumps are aliased in most observations); 2) pore-scale Haines jumps do not necessarily define macroscale invasion patterns; and 3) viscous fingers reach a characteristic length scale. On the other hand, dissolution wormholes can grow beyond the scale of the engineering problem under consideration. In some cases, the upscaling of local instabilities to global instabilities will depend on global properties such as spatial variability in grain size, pore size, mineralogy, and contact forces.

5 CONCLUSION

Fluid-driven instabilities are ubiquitous in soils and sediments. However, they are often overlooked in the interpretation of laboratory studies as well as in analytical solutions and numerical simulations. These instabilities can emerge across scales and are readily observed in millimeter-scale microfluidic chips to kilometer-scale features in the geological record.

Some fluid-driven instabilities take place within the pore space without affecting the granular skeleton. These instabilities are driven by differences in viscosity between the invading and the defending fluids, interfacial tension, and capillarity and cause characteristic invasion patterns. Pore-scale capillary instabilities result from a combination of hysteresis in contact angle and interfacial tension, elastic deformations, and the longitudinal pore geometry. Sudden jumps in fluid interfaces and

associated snap-offs cause rapid redistribution of phases. Particle-laden fluids may also cause instabilities in rigid porous media.

More intricate instabilities take place when fluids affect the granular skeleton. In general, hydro-thermo-chemo-mechanically coupled processes affect the sediment structure and can cause instabilities under certain conditions.

Fluid-driven instabilities coupled with fabric changes can be generated by viscous forces in single-phase fluid injection (hydraulic fracture) or by capillary forces produced by an immiscible fluid (grain-displacive invasion: desiccation cracks, ice and hydrate lenses, gas and oil-driven openings, and capillary collapse). The marked differences between viscosity and capillarity-driven open-mode discontinuities require careful analysis prior to numerical modeling.

Mineral dissolution caused by the injection of reactive fluids evolves as a function of the interplay between various rates (advection, diffusion, and reaction), the spatial distribution of reactive minerals, and the granular skeleton response during dissolution. Instabilities include wormhole formation and the emergence of shear bands (even in sediments under zero lateral strain conditions).

Other fluid-driven instabilities in granular materials are associated with particle transport (piping erosion), thermal

changes (thermo-hydraulic fractures), and changes in electrical interparticle interaction (osmotic-hydraulic fractures and contractive openings).

In all cases, instabilities involve some form of positive feedback mechanism; conversely, self-homogenizing processes tend to be stabilizing for fluid flow and granular stability. The types of instabilities and their evolving topologies can be systematically organized in the space defined by dimensionless ratios of time (or rate), length scales, and forces (or pressure and stress).

AUTHOR CONTRIBUTIONS

All authors listed have made a substantial, direct, and intellectual contribution to the work and approved it for publication.

ACKNOWLEDGMENTS

G. Abelskamp edited the manuscript. M. Benitez obtained the hysteretic interfacial tension and contact angle data. Support for this research was provided by the KAUST Endowment.

REFERENCES

- Al-Arji, H., Al-Azman, A., Le-Hussain, F., and Regenauer-Lieb, K. (2021). Acid Stimulation in Carbonates: A Laboratory Test of a Wormhole Model Based on Damköhler and Péclet Numbers. *J. Petroleum Sci. Eng.* 203, 108593. doi:10.1016/j.petrol.2021.108593
- Al-Sahhaf, T., Elkamel, A., Suttar Ahmed, A., and Khan, A. R. (2005). The Influence of Temperature, Pressure, Salinity, and Surfactant Concentration on the Interfacial Tension of the N-Octane-Water System. *Chem. Eng. Commun.* 192, 667–684. doi:10.1080/009864490510644
- An, S., Erfani, H., Godínez-Brizuela, O. E., and Niasar, V. (2020). Transition From Viscous Fingering to Capillary Fingering: Application of GPU-Based Fully Implicit Dynamic Pore Network Modeling. *Water Resour. Res.* 56 (12), e2020WR028149. doi:10.1029/2020WR028149
- Andújar Márquez, J., Martínez Bohórquez, M., and Gómez Melgar, S. (2016). Ground Thermal Diffusivity Calculation by Direct Soil Temperature Measurement. Application to Very Low Enthalpy Geothermal Energy Systems. *Sensors* 16, 306. doi:10.3390/s16030306
- Bachu, S., and Bennion, D. B. (2009). Interfacial Tension between CO₂, Freshwater, and Brine in the Range of Pressure from (2 to 27) MPa, Temperature from (20 to 125) °C, and Water Salinity from (0 to 334 000) mg-L⁻¹. *J. Chem. Eng. Data* 54, 765–775. doi:10.1021/je800529x
- Barden, L., McGown, A., and Collins, K. (1973). The Collapse Mechanism in Partly Saturated Soil. *Eng. Geol.* 7, 49–60. doi:10.1016/0013-7952(73)90006-9
- Bardet, J. P., and Kapuskar, M. (1993). Liquefaction Sand Boils in San Francisco during 1989 Loma Prieta Earthquake. *J. Geotech. Engrg.* 119, 543–562. doi:10.1061/(asce)0733-9410(1993)119:3(543)
- Benitez, M. D. (2022). Complex Fluids for Geo-Energy Applications. PhD thesis.
- Berg, S., Ott, H., Klapp, S. A., Schwing, A., Neiteler, R., Brussee, N., et al. (2013). Real-time 3D Imaging of Haines Jumps in Porous Media Flow. *Proc. Natl. Acad. Sci. U.S.A.* 110, 3755–3759. doi:10.1073/pnas.1221373110
- Berney, E. S. (2004). A Partially Saturated Constitutive Theory for Compacted Fills. Available at: <https://apps.dtic.mil/sti/citations/ADA425462> (Accessed April 26, 2022). doi:10.21236/ada425462
- Bruchon, J.-F., Pereira, J.-M., Vandamme, M., Lenoir, N., Delage, P., and Bornert, M. (2013). Full 3D Investigation and Characterisation of Capillary Collapse of a changes (thermo-hydraulic fractures), and changes in electrical interparticle interaction (osmotic-hydraulic fractures and contractive openings).
- Loose Unsaturated Sand Using X-Ray CT. *Granul. Matter* 15, 783–800. doi:10.1007/s10035-013-0452-6
- Cardona, A., Finkbeiner, T., and Santamarina, J. C. (2021). Natural Rock Fractures: From Aperture to Fluid Flow. *Rock Mech. Rock Eng.* 54, 5827–5844. doi:10.1007/s00603-021-02565-1
- Carrillo, F. J., and Bourg, I. C. (2021). Capillary and Viscous Fracturing during Drainage in Porous Media. *Phys. Rev. E* 103, 063106. doi:10.1103/PhysRevE.103.063106
- Cartwright, J. A., and Dewhurst, D. N. (1998). Layer-bound Compaction Faults in Fine-Grained Sediments. *Geol. Soc. Am. Bull.* 110, 1242–1257. doi:10.1130/0016-7606(1998)110<1242:lbcf>2.3.co;2
- Cartwright, J., and Santamarina, C. (2015). Seismic Characteristics of Fluid Escape Pipes in Sedimentary Basins: Implications for Pipe Genesis. *Mar. Petroleum Geol.* 65, 126–140. doi:10.1016/j.marpetgeo.2015.03.023
- Castro, G. M., Park, J., and Santamarina, J. C. (2022). Revised Soil Classification System RSCS: Implementation and Engineering Implications. *Submitt. Publ.*
- Cha, M., and Santamarina, J. C. (2014). Dissolution of Randomly Distributed Soluble Grains: Post-dissolution K₀-Loading and Shear. *Géotechnique* 64, 828–836. doi:10.1680/geot.14.p.115
- Cha, M., and Santamarina, J. C. (2016). Hydro-chemo-mechanical Coupling in Sediments: Localized Mineral Dissolution. *Geomechanics Energy Environ.* 7, 1–9. doi:10.1016/j.gete.2016.06.001
- Cha, M., and Santamarina, J. C. (2019a). Localized Dissolution in Sediments under Stress. *Granul. Matter* 21, 79. doi:10.1007/s10035-019-0932-4
- Cha, M., and Santamarina, J. C. (2019b). Pressure-dependent Grain Dissolution Using Discrete Element Simulations. *Granul. Matter* 21, 101. doi:10.1007/s10035-019-0960-0
- Chameau, J. L., Clough, G. W., Reyna, F., and Frost, J. D. (1991). Liquefaction Response of San Francisco Bayshore Fills. *Bull. Seismol. Soc. Am.* 81, 1998–2018. doi:10.1785/BSSA0810051998
- Chand, S., Thorsnes, T., Rise, L., Brunstad, H., Stoddart, D., Bøe, R., et al. (2012). Multiple Episodes of Fluid Flow in the SW Barents Sea (Loppa High) Evidenced by Gas Flares, Pockmarks and Gas Hydrate Accumulation. *Earth Planet. Sci. Lett.* 331–332, 305–314. doi:10.1016/j.epsl.2012.03.021
- Chang, C. H., and Franses, E. I. (1992). Modified Langmuir-Hinselwood Kinetics for Dynamic Adsorption of Surfactants at the Air/water Interface. *Colloids Surfaces* 69, 189–201. doi:10.1016/0166-6622(92)80230-Y

- Chang, D. S., and Zhang, L. M. (2013). Extended Internal Stability Criteria for Soils under Seepage. *Soils Found.* 53, 569–583. doi:10.1016/j.sandf.2013.06.008
- Chatzis, I., and Morrow, N. R. (1984). Correlation of Capillary Number Relationships for Sandstone. *Soc. Pet. Eng. J.* 24, 555–562. doi:10.2118/10114-pa
- Cordero, J. A., Useche, G., Prat, P. C., Ledesma, A., and Santamarina, J. C. (2017). Soil Desiccation Cracks as a Suction-Contraction Process. *Géotechnique Lett.* 7, 279–285. doi:10.1680/jgele.17.00070
- Croizé, D., Renard, F., Bjørlykke, K., and Dysthe, D. K. (2010). Experimental Calcite Dissolution under Stress: Evolution of Grain Contact Microstructure during Pressure Solution Creep. *J. Geophys. Res.* 115 (B9). doi:10.1029/2010JB000869
- Dai, S., Santamarina, J. C., Waite, W. F., and Kneafsey, T. J. (2012). Hydrate Morphology: Physical Properties of Sands with Patchy Hydrate Saturation. *J. Geophys. Res.* 117, B11205. doi:10.1029/2012JB009667
- Dawson, H. E., and Roberts, P. V. (1997). Influence of Viscous, Gravitational, and Capillary Forces on DNAPL Saturation. *Groundwater* 35, 261–269. doi:10.1111/j.1745-6584.1997.tb00083.x
- de Gennes, P.-G. (1985). Wetting: Statics and Dynamics. *Rev. Mod. Phys.* 57, 827–863. doi:10.1103/revmodphys.57.827
- Derr, N. J., Fronk, D. C., Weber, C. A., Mahadevan, A., Rycroft, C. H., and Mahadevan, L. (2020). Flow-Driven Branching in a Frangible Porous Medium. *Phys. Rev. Lett.* 125, 158002. doi:10.1103/PhysRevLett.125.158002
- Dreybrodt, W. (1990). The Role of Dissolution Kinetics in the Development of Karst Aquifers in Limestone: a Model Simulation of Karst Evolution. *J. Geol.* 98, 639–655. doi:10.1086/629431
- Eral, H. B., 't Mannetje, D. J. C. M., and Oh, J. M. (2013). Contact Angle Hysteresis: A Review of Fundamentals and Applications. *Colloid Polym. Sci.* 291, 247–260. doi:10.1007/s00396-012-2796-6
- Etheridge, M. A., Wall, V. J., Cox, S. F., and Vernon, R. H. (1984). High Fluid Pressures During Regional Metamorphism and Deformation: Implications for Mass Transport and Deformation Mechanisms. *J. Geophys. Res.* 89, 4344–4358. doi:10.1029/jb089ib06p04344
- Fannin, R. J., Arulrajah, A., Slangen, P., Evans, R., Arulrajah, A., and Evans, R. (2015). Discussion: On the Distinct Phenomena of Suffusion and Suffosion. *Geotech. Lett.* 5, 129–130. doi:10.1680/jgele.15.0001710.1680/geolett.15.00017
- Ferer, M., Ji, C., Bromhal, G. S., Cook, J., Ahmadi, G., and Smith, D. H. (2004). Crossover from Capillary Fingering to Viscous Fingering for Immiscible Unstable Flow: Experiment and Modeling. *Phys. Rev. E* 70, 16303. doi:10.1103/PhysRevE.70.16303
- Fowler, A. C., and Yang, X. (1999). Pressure Solution and Viscous Compaction in Sedimentary Basins. *J. Geophys. Res.* 104, 12989–12997. doi:10.1029/1998jb900029
- Freddi, C. N. (2000). Dynamic Model of Wormhole Formation Demonstrates Conditions for Effective Skin Reduction During Carbonate Matrix Acidizing. *SPE Permian Basin Oil Gas. Recover. Conf. Proc.* doi:10.2118/59537-ms
- Freddi, C. N., and Fogler, H. S. (1998). Influence of Transport and Reaction on Wormhole Formation in Porous Media. *AIChE J.* 44, 1933–1949. doi:10.1002/aic.690440902
- Frost, J. D., Roy, N., Chen, C.-C., Park, J.-Y., Jang, D.-J., Lu, Y., et al. (2019). Quantitative Analysis of Microstructure Properties and Their Influence on Macroscale Response. *KSCCE J. Civ. Eng.* 23, 3777–3792. doi:10.1007/S12205-019-0713-Y
- Gao, N., Geyer, F., Pilat, D. W., Wooh, S., Vollmer, D., Butt, H.-J., et al. (2018). How Drops Start Sliding over Solid Surfaces. *Nat. Phys.* 14, 191–196. doi:10.1038/nphys4305
- Gauglitz, P. A., and Radke, C. J. (1989). Dynamics of Haines Jumps for Compressible Bubbles in Constricted Capillaries. *AIChE J.* 35, 230–240. doi:10.1002/aic.690350207
- Gibbs, J. W. (1878). On the Equilibrium of Heterogeneous Substances. *Am. J. Sci.* s3-16, 441–458. doi:10.2475/ajs.s3-16.96.441
- Golfier, F., Zarccone, C., Bazin, B., Lenormand, R., Lasseux, D., and Quintard, M. (2002). On the Ability of a Darcy-Scale Model to Capture Wormhole Formation during the Dissolution of a Porous Medium. *J. Fluid Mech.* 457, 213–254. doi:10.1017/S0022112002007735
- He, Y., Yazhgur, P., Salonen, A., and Langevin, D. (2015). Adsorption-desorption Kinetics of Surfactants at Liquid Surfaces. *Adv. Colloid Interface Sci.* 222, 377–384. doi:10.1016/j.cis.2014.09.002
- Helfrich, K. R. (1995). Thermo-viscous Fingering of Flow in a Thin Gap: A Model of Magma Flow in Dikes and Fissures. *J. Fluid Mech.* 305, 219–238. doi:10.1017/S0022112095004605
- Hendron, A. (2013). Improving Dam Safety with Lessons Learned from Case Histories of Dam Failures and Unacceptable Dam Performance. *Karl Terzaghi Lect.*
- Holtzman, R., Szulczewski, M. L., and Juanes, R. (2012). Capillary Fracturing in Granular Media. *Phys. Rev. Lett.* 108, 264504. doi:10.1103/PhysRevLett.108.264504
- Houston, S. L., Houston, W. N., and Spadola, D. J. (1988). Prediction of Field Collapse of Soils Due to Wetting. *J. Geotechnical Eng.* 114114, 401–458. doi:10.1061/(asce)0733-9410(1988)114:1(40)
- Hovland, M., Gardner, J. V., and Judd, A. G. (2002). The Significance of Pockmarks to Understanding Fluid Flow Processes and Geohazards. *Geofluids* 2, 127–136. doi:10.1046/j.1468-8123.2002.00028.x
- Hua, X., Bevan, M. A., and Frechette, J. (2016). Reversible Partitioning of Nanoparticles at an Oil-Water Interface. *Langmuir* 32, 11341–11352. doi:10.1021/ACS.LANGMUIR.6B02255
- Ishihara, K. (1993). Liquefaction and Flow Failure during Earthquakes. *Géotechnique* 43, 351–451. doi:10.1680/geot.1993.43.3.351
- Ishihara, K. (1997). Soil Behaviour in Earthquake Geotechnics. *Choice Rev. Online* 34, 5113. doi:10.5860/choice.34-5113
- Islam, M. N., and Azaiez, J. (2010). Miscible Thermo-Viscous Fingering Instability in Porous Media. Part 1: Linear Stability Analysis. *Transp. Porous Med.* 84, 821–844. doi:10.1007/s11242-010-9555-2
- Jang, J., Narsilio, G. A., and Santamarina, J. C. (2011). Hydraulic Conductivity in Spatially Varying Media-A Pore-Scale Investigation. *Geophys. J. Int.* 184, 1167–1179. doi:10.1111/j.1365-246X.2010.04893.x
- Jang, J., and Santamarina, J. C. (2014). Evolution of Gas Saturation and Relative Permeability during Gas Production from Hydrate-Bearing Sediments: Gas Invasion vs. Gas Nucleation. *J. Geophys. Res. Solid Earth* 119, 116–126. doi:10.1002/2013JB010480
- Jang, J., Sun, Z., and Santamarina, J. C. (2016). Capillary Pressure across a Pore Throat in the Presence of Surfactants. *Water Resour. Res.* 52, 9586–9599. doi:10.1002/2015WR018499
- Jung, J.-W., Santamarina, J. C., and Soga, K. (2012). Stress-strain Response of Hydrate-Bearing Sands: Numerical Study Using Discrete Element Method Simulations. *J. Geophys. Res.* 117, 4202. doi:10.1029/2011JB009040
- Kim, J., Xu, F., and Lee, S. (2017). Formation and Destabilization of the Particle Band on the Fluid-Fluid Interface. *Phys. Rev. Lett.* 118, 074501. doi:10.1103/PhysRevLett.118.074501
- Kim, S., and Santamarina, J. C. (2015). Reactive Fluid Flow in CO₂ Storage Reservoirs: A 2-D Pore Network Model Study. *Greenh. Gas. Sci. Technol.* 5, 462–473. doi:10.1002/ghg.1487
- Kochmann, D. M., and Bertoldi, K. (2017). Exploiting Microstructural Instabilities in Solids and Structures: From Metamaterials to Structural Transitions. *Appl. Mech. Rev.* 69 (5). doi:10.1115/1.4037966
- Lange, A., Schröter, M., Scherer, M. A., Engel, A., and Rehberg, I. (1998). Fingering Instability in a Water-Sand Mixture. *Eur. Phys. J. B* 4, 475–484. doi:10.1007/s100510050405
- Langmuir, I. (1918). The Adsorption of Gases on Plane Surfaces of Glass, Mica and Platinum. *J. Am. Chem. Soc.* 40, 1361–1403. doi:10.1021/ja02242a004
- Lee, J.-S., and Santamarina, J. C. (2007). Seismic Monitoring Short-Duration Events: Liquefaction in Igmodels. *Can. Geotech. J.* 44, 659–672. doi:10.1139/T07-020
- Lei, L., and Santamarina, J. C. (2018). Laboratory Strategies for Hydrate Formation in Fine-Grained Sediments. *J. Geophys. Res. Solid Earth* 123, 2583–2596. doi:10.1002/2017JB014624
- Lenormand, R., Touboul, E., and Zarccone, C. (1988). Numerical Models and Experiments on Immiscible Displacements in Porous Media. *J. Fluid Mech.* 189, 165–187. doi:10.1017/s0022112088000953
- Lenormand, R., Zarccone, C., and Sarr, A. (1983). Mechanisms of the Displacement of One Fluid by Another in a Network of Capillary Ducts. *J. Fluid Mech.* 135, 337–353. doi:10.1017/S0022112083003110
- Li, M., and Fannin, R. J. (2008). Comparison of Two Criteria for Internal Stability of Granular Soil. *Can. Geotech. J.* 45, 1303–1309. GIF. doi:10.1139/T08-046/ASSET/IMAGES/T08-046IE17H
- Li, P., Vanapalli, S., and Li, T. (2016). Review of Collapse Triggering Mechanism of Collapsible Soils Due to Wetting. *J. Rock Mech. Geotechnical Eng.* 8, 256–274. doi:10.1016/j.jrmge.2015.12.002
- Liot, O., Singh, A., Bacchin, P., Duru, P., Morris, J. F., and Joseph, P. (2018). Pore Cross-Talk in Colloidal Filtration. *Sci. Rep.* 8, 12460. doi:10.1038/s41598-018-30389-7
- Liu, Q., Sun, Z., and Santamarina, J. C. (2021). Self-assembled Nanoparticle-Coated Interfaces: Capillary Pressure, Shell Formation and Buckling. *J. Colloid Interface Sci.* 581, 251–261. doi:10.1016/j.jcis.2020.07.110
- Liu, Q., Zhao, B., and Santamarina, J. C. (2019). Particle Migration and Clogging in Porous Media: A Convergent Flow Microfluidics Study. *J. Geophys. Res. Solid Earth* 124, 9495–9504. doi:10.1029/2019JB017813

- Menke, H. P., Bijeljic, B., and Blunt, M. J. (2017). Dynamic Reservoir-Condition Microtomography of Reactive Transport in Complex Carbonates: Effect of Initial Pore Structure and Initial Brine pH. *Geochimica Cosmochimica Acta* 204, 267–285. doi:10.1016/j.gca.2017.01.053
- Meyer, E. E., Rosenberg, K. J., and Israelachvili, J. (2006). Recent Progress in Understanding Hydrophobic Interactions. *Proc. Natl. Acad. Sci. U.S.A.* 103, 15739–15746. doi:10.1073/pnas.0606422103
- Mitchell, J. K. (1991). Conduction Phenomena: From Theory to Geotechnical Practice. *Geotechnique* 41, 299–340. doi:10.1680/geot.1991.41.3.299
- Mitchell, J. K. (1976). *Fundamental of Soil Behaviour*. Hoboken, New Jersey, United States: John Wiley & Sons.
- Moffat, R., Fannin, R. J., and Garner, S. J. (2011). Spatial and Temporal Progression of Internal Erosion in Cohesionless Soil. *Can. Geotech. J.* 48, 399–412. doi:10.1139/t10-071
- Morrow, N. R., and Szabo, J. O. (1970). Physics and Thermodynamics of Capillary Action in Porous Media. *Ind. Eng. Chem.* 62, 32–56. doi:10.1021/ie50726a006
- Moss, J. L., Cartwright, J., and Moore, R. (2012). Evidence for Fluid Migration Following Pockmark Formation: Examples from the Nile Deep Sea Fan. *Mar. Geol.* 303–306, 1–13. doi:10.1016/j.margeo.2012.01.010
- Mulligan, C. N., Yong, R. N., and Gibbs, B. F. (2001). Surfactant-enhanced Remediation of Contaminated Soil: a Review. *Eng. Geol.* 60, 371–380. doi:10.1016/S0013-7952(00)00117-4
- National Academies of Sciences and Medicine, E (2020). *Characterization, Modeling, Monitoring, and Remediation of Fractured Rock*. Washington, D.C., United States: National Academies Press.
- Peña, T. J., Carvalho, M. S., and Alvarado, V. (2009). Snap-off of a Liquid Drop Immersed in Another Liquid Flowing through a Constricted Capillary. *AIChE J.* 55, 1993–1999. doi:10.1002/aic.11839
- Rebata-Landa, V., and Santamarina, J. C. (2012). Mechanical Effects of Biogenic Nitrogen Gas Bubbles in Soils. *J. Geotech. Geoenviron. Eng.* 138, 128–137. doi:10.1061/(asce)gt.1943-5606.0000571
- Robbins, B. A., and Van Beek, V. M. (2015). Backward Erosion Piping: A Historical Review and Discussion of Influential Factors. *Assoc. State Dam Saf. Off. Dam Saf.* 2, 919–938.
- Romanov, D., Gabrovšek, F., and Dreybrodt, W. (2003). Dam Sites in Soluble Rocks: A Model of Increasing Leakage by Dissolution Widening of Fractures beneath a Dam. *Eng. Geol.* 70, 17–35. doi:10.1016/S0013-7952(03)00073-5
- Rutter, E. H. (1983). Pressure Solution in Nature, Theory and Experiment. *J. Geol. Soc.* 140, 725–740. doi:10.1144/gsjgs.140.5.0725
- Sandnes, B., Flekkøy, E. G., Knudsen, H. A., Måløy, K. J., and See, H. (2011). Patterns and Flow in Frictional Fluid Dynamics. *Nat. Commun.* 2, 288. doi:10.1038/ncomms1289
- Santamarina, J. C., and Jang, J. (2011). Energy Geotechnology: Implications of Mixed Fluid Conditions. Available at: https://egel.kaust.edu.sa/Documents/Papers/Santamarina_2010a.pdf (Accessed September 29, 2019).
- Santamarina, J. C. (2003). Soil Behavior at the Microscale: Particle Forces. *Geotechnical-Special-Publication*, 25–56. doi:10.1061/40659(2003)2
- Santamarina, J. C., Torres-Cruz, L. A., and Bachus, R. C. (2019). Why Coal Ash and Tailings Dam Disasters Occur. *Science*. 364, 526–528. doi:10.1126/SCIENCE.AAX1927
- Schneider, J. A., and Mayne, P. W. (2000). “Liquefaction Response of Soils in Mid-America Evaluated by Seismic Cone Tests,” in *Innovations and Applications In Geotechnical Site Characterization* (Denver, CO: Geo), 1–16.
- Sherard, J. L. (1987). Lessons from the Teton Dam Failure. *Eng. Geol.* 24, 239–256. doi:10.1016/0013-7952(87)90064-0
- Shin, H., Santamarina, J. C., and Cartwright, J. A. (2008). Contraction-driven Shear Failure in Compacting Uncemented Sediments. *Geol* 36, 931–934. doi:10.1130/g24951a.1
- Shin, H., and Santamarina, J. C. (2011a). Desiccation Cracks in Saturated Fine-Grained Soils: Particle-Level Phenomena and Effective-Stress Analysis. *Geotechnique* 61, 961–972. doi:10.1680/geot.8.P.012
- Shin, H., and Santamarina, J. C. (2010). Fluid-driven Fractures in Uncemented Sediments: Underlying Particle-Level Processes. *Earth Planet. Sci. Lett.* 299, 180–189. doi:10.1016/j.epsl.2010.08.033
- Shin, H., and Santamarina, J. C. (2009). Mineral Dissolution and the Evolution of K₀. *J. Geotech. Geoenviron. Eng.* 135, 1141–1147. doi:10.1061/(ASCE)GT.1943-5606.0000053
- Shin, H., and Santamarina, J. C. (2011b). Open-mode Discontinuities in Soils. *Geotechnique Lett.* 1, 95–99. doi:10.1680/geolett.11.00014
- Sills, G. C., Wheeler, S. J., Thomas, S. D., and Gardner, T. N. (1991). Behaviour of Offshore Soils Containing Gas Bubbles. *Geotechnique* 41, 227–241. doi:10.1680/geot.1991.41.2.227
- Skempton, A. W., and Brogan, J. M. (1994). Experiments on Piping in Sandy Gravels. *Geotechnique* 44, 449–460. doi:10.1680/geot.1994.44.3.449
- Sparks, A. D. W., Gallipoli, D., Augarde, C. E., Toll, D. G., Fisher, P. C., and Congreve, A. (2012). Formation and Evolution of Water Menisci in Unsaturated Granular Media. *Geotechnique* 62, 1143–1144. doi:10.1680/geot.12.D.004
- Sukkarak, R., Tanapalungkorn, W., Likitlersuang, S., and Ueda, K. (2021). Liquefaction Analysis of Sandy Soil during Strong Earthquake in Northern Thailand. *Soils Found.* 61, 1302–1318. doi:10.1016/j.sandf.2021.07.003
- Sun, Z., Liu, Q., Benitez, M. D., and Santamarina, J. C. (2022). Invasion Patterns Induced by Nanoparticle-Coated Interfaces. *Under Prep.*
- Sun, Z., and Santamarina, J. C. (2019a). Grain-Displacive Gas Migration in Fine-Grained Sediments. *J. Geophys. Res. Solid Earth* 124, 2274–2285. doi:10.1029/2018JB016394
- Sun, Z., and Santamarina, J. C. (2019b). Haines Jumps: Pore Scale Mechanisms. *Phys. Rev. E* 100, 023115. doi:10.1103/physreve.100.023115
- Valdes, J. R., and Carlos Santamarina, J. (2007). Particle Transport in a Nonuniform Flow Field: Retardation and Clogging. *Appl. Phys. Lett.* 90, 244101. doi:10.1063/1.2748850
- Valdes, J. R., and Santamarina, J. C. (2006). Particle Clogging in Radial Flow: Microscale Mechanisms. *SPE J.* 11, 193–198. doi:10.2118/88819-PA
- Van Zwieten, R., Van De Laar, T., Sprakel, J., and Schroën, K. (2018). From Cooperative to Uncorrelated Clogging in Cross-Flow Microfluidic Membranes. *Sci. Rep.* 8, 5687. doi:10.1038/s41598-018-24088-6
- Viggiani, G., Andò, E., Takano, D., and Santamarina, J. C. (2014). Laboratory X-Ray Tomography: A Valuable Experimental Tool for Revealing Processes in Soils. *Geotech. Test. J.* 38, 20140060–20140071. doi:10.1520/GTJ20140060
- Völtz, C., Pesch, W., and Rehberg, I. (2002). Rayleigh-Taylor Instability in a Sedimenting Suspension. *Phys. Rev. E* 65, 011404. doi:10.1103/PhysRevE.65.011404
- Weyl, P. K. (1959). Pressure Solution and the Force of Crystallization: a Phenomenological Theory. *J. Geophys. Res.* 64, 2001–2025. doi:10.1029/jz064i011p02001
- Young, T. (1805). III. An Essay on the Cohesion of Fluids. *Phil. Trans. R. Soc.* 95, 65–87. doi:10.1098/rstl.1805.0005
- Yun, T. S. (2005). Mechanical and Thermal Study of Hydrate Bearing Sediments. PhD Thesis. Available at: <https://libproxy.kaust.edu.sa/login?url=https://www.proquest.com/dissertations-theses/mechanical-thermal-study-hydrate-bearing/docview/304999500/se-2?accountid=78788>.
- Zhao, B., MacMinn, C. W., and Juanes, R. (2016). Wettability Control on Multiphase Flow in Patterned Microfluidics. *Proc. Natl. Acad. Sci. U.S.A.* 113, 10251–10256. doi:10.1073/pnas.1603387113
- Zhao, B., MacMinn, C. W., Prinkulov, B. K., Chen, Y., Valocchi, A. J., Zhao, J., et al. (2019). Comprehensive Comparison of Pore-Scale Models for Multiphase Flow in Porous Media. *Proc. Natl. Acad. Sci. U.S.A.* 116, 13799–13806. doi:10.1073/pnas.1901619116
- Zhao, B., and Santamarina, J. C. (2020). Desiccation Crack Formation beneath the Surface. *Geotechnique* 70, 181–186. doi:10.1680/jgeot.18.T.019

Conflict of Interest: The authors declare that the research was conducted in the absence of any commercial or financial relationships that could be construed as a potential conflict of interest.

Publisher’s Note: All claims expressed in this article are solely those of the authors and do not necessarily represent those of their affiliated organizations, or those of the publisher, the editors, and the reviewers. Any product that may be evaluated in this article, or claim that may be made by its manufacturer, is not guaranteed or endorsed by the publisher.

Copyright © 2022 Liu and Santamarina. This is an open-access article distributed under the terms of the Creative Commons Attribution License (CC BY). The use, distribution or reproduction in other forums is permitted, provided the original author(s) and the copyright owner(s) are credited and that the original publication in this journal is cited, in accordance with accepted academic practice. No use, distribution or reproduction is permitted which does not comply with these terms.

GLOSSARY

- A_h [J]** Hamaker constant in van der Waals interaction
- A [N/m]** contact line adhesion
- Ar []** Archimedes number
- Bo []** bond number
- C [mol/L]** concentration
- c_v [m^2/s]** pressure diffusion coefficient
- Ca []** capillary number
- d [m]** diameter
- D [m^2/s]** diffusion coefficient
- D_T [m^2/s]** thermal diffusion coefficient
- Da []** Damköhler number
- e []** void ratio
- F [N]** force (c: capillary; b: buoyant; D: drag; sk: skeletal; W: grain weight; EL: electrical interaction; wall: wall interaction; Th: thermo-elastic)
- g [m/s^2]** standard gravity
- G [Pa/m^3]** stiffness (sk: skeleton)
- H [m]** height
- k [1/s]** kinetic rate of reaction
- K [Pa/m^3]** system stiffness
- k_0 []** lateral earth pressure coefficient at rest
- L [m]** characteristic length
- L_{ch} [m]** channel length
- LL []** liquid limit
- M []** viscous ratio
- N_{ad} []** contact number
- N_{ec} []** elastocapillary number
- u [Pa]** fluid pressure (w: wetting phase; n: non-wetting phase)
- Pe []** Péclet number
- r [m]** pore radius
- Stk []** Stokes number
- t [s]** time scale (adv: advection; diff: diffusion; r: reaction; in: inertia)
- V [m^3]** volume
- W []** water content
- z [m]** depth
- v [m/s]** fluid flow velocity
- Δu [Pa]** capillary pressure
- α [°]** local pore wall angle
- α_{sk} [$1/^\circ C$]** thermal expansion coefficient of the skeleton
- γ [N/m]** interfacial tension (VS.: vapor-solid; LS: liquid-solid; LV: liquid-vapor)
- θ [°]** contact angle (a: advancing; r: receding)
- μ [Pa.s]** viscosity (inv: invading phase; def: defending phase)
- Π_{inv} []** dimensionless ratio: capillary force over skeletal force
- Π_{drag} []** dimensionless ratio: drag force over skeletal force
- Π_{THM} []** dimensionless ratio between thermal diffusion and pressure diffusion
- ρ [kg/m^3]** density (b: buoyant; w: water; p: particle; f: fluid)
- σ' [Pa]** effective stress
- Γ [mol/m^2]** surface excess concentration